Transient Brittle Creep mechanism explains early postseismic phase of the 2011 Tohoku-Oki megathrust earthquake: observations by high-rates GPS solutions

Axel Periollat[*1], Mathilde Radiguet[1], Jérôme Weiss[1], Cédric Twardzik[2], David Amitrano[1], Nathalie Cotte[1], Lou Marill[1], and Anne Socquet[1]

[1] Univ. Grenoble Alpes, Univ. Savoie Mont Blanc, CNRS, IRD, Univ. Gustave Eiffel, ISTerre, 38000 Grenoble, France
[2] Institut de Physique du Globe de Strasbourg, UMR 7516, Université de Strasbourg, EOST, CNRS, Strasbourg, France

Corresponding author: Axel Periollat (axel.periollat@univ-grenoble-alpes.fr)

Key Points:

- Kinematic and static positions time series are used to analyse the postseismic deformation following the M_w 9.0 Tohoku-Oki earthquake
- The temporal evolution of the early postseismic is explained by an Omori-like Transient Brittle Creep mechanism with a *p*-value around 0.75
- The spatial analysis reveals a major afterslip zone downdip from the main rupture and a secondary one close to the Ibaraki-Oki event

Abstract

The early stage of the postseismic phase is characterized by a large deformation rate. Its analysis is thus key to decipher the role played by different mechanisms (afterslip and viscoelasticity) at various time scales. Here, we process GPS data to obtain 30-seconds kinematic position time series recording the surface deformation following the Mw 9.0 Tohoku-Oki megathrust earthquake (2011), and combine them with static solutions over 9 years. We analyze the temporal evolution of the time series and use these observations to image the postseismic slip. We find that the first month of deformation following Tohoku-Oki can be explained by an afterslip mechanism, that exhibits an "Omori-like" decay, with a *p*-value around 0.75 almost everywhere with the exception of a small region around Ibaraki prefecture where $p \sim 1$ is observed. This $p<1$ indicates that the postseismic displacements do not increase logarithmically with time as predicted by rate-and-state rheology. Instead, we argue that early afterslip is associated to a transient brittle creep mechanism. We use numerical simulations to show that an exponent of $p<1$ can be explained by a combination of thermal activation of local slips and elastic interactions. Over longer time scales, an additional mechanism is required to explain the observed deformation signal, and the transient brittle creep mechanism is combined with viscoelastic relaxation modeled by a Newtonian flow. The spatial analysis reveals two distinct afterslip regions, a major one on the North, associated with a *p*-value around 0.75, and a smaller one close to the Ibaraki aftershock, associated to $p \sim 1$.

Plain Language Summary

The Tohoku-Oki earthquake of March 11, 2011, is one of the largest subduction earthquake of the past decade. Earthquakes produce a perturbation in the state of the stress of the crust and mantle, and this perturbation is relaxed after the earthquake, during the postseismic phase. This phase is associated with deformations measurable at the earth surface with instruments such as GPS stations. These measurements can be used to infer the different processes involved in this relaxation, among which the one called afterslip, which corresponds to the aseismic slip that occur at depth around the fault zone. The originality of our study is the inclusion of the GPS signal from the first few minutes, to constrain the details of the early postseismic deformation. We find that the early postseismic phase could be described by a different modeling than the one commonly used by the community with an evolution as a logarithm of time. We have identified a major region downdip of the Tohoku-Oki rupture zone and another small area near the large aftershock is identified with different temporal evolution. Further studies on large earthquakes should consider these results to revisit and review the early postseismic phase after large subduction earthquakes.

1 Introduction

Following large earthquakes, the state of stress of the surrounding earth crust and mantle is modified, triggering aftershocks and various aseismic processes, in the so called postseismic phase. Aftershocks represent a small portion of the energy released in this postseismic phase, and aseismic processes, among which afterslip (transient frictional sliding on the fault), mantellic viscoelastic relaxation in the mantle, and/or poroelastic rebound are considered to dominate. These mechanisms involve different spatial and temporal scales, and it is not trivial to differentiate between them based on the deformation signal observed at the surface (Ingleby & Wright, 2017).

A detailed analysis of the temporal evolution of the deformation is necessary to identify the underlying mechanisms at play at both short (minutes to days) and long (years) timescales. The early stages of the postseismic phase, from a few minutes to a few hours after the mainshock, are characterized by high deformation rates. Analyzing the deformation in this early period can bring strong constraints on the postseismic behavior. Yet, the early postseismic deformation has been little studied, because high-rate time series of the surface deformation in the vicinity of the rupture zone are not easily available and, when available, it is complex to detect signal at this early stage due to the larger noise level of the high-rate time series compared to traditional daily position time series (Twardzik et al., 2019).

The recent devastating megathrusts earthquakes (Sumatra, Chile and Japan) significantly increased our understanding of the postseismic phase. In particular, the M_w 9.0 Tohoku earthquake was recorded with unprecedented high resolution is space and time, and provides a unique opportunity to analyze the postseismic relaxation, including in its early stage. For these large subduction earthquakes, afterslip and viscoelastic relaxation have been identified as the most important mechanisms (*e.g.* Wang et al., 2012) to explain the observed deformation. Instead, the contribution of the poroelastic rebound to the inland displacement was shown to be small for the Tohoku-Oki event (Hu et al., 2014).

Deciphering the contributions of afterslip and viscoelastic relaxation in the postseismic deformation signal, notably in the early stages remains a difficult problem. Postseismic models assuming an elastic earth (Ozawa et al., 2012) tend to substantially overestimate the amount of afterslip compared to viscoelastic models including a transient viscosity (Sun et al., 2014; Sun & Wang, 2015). Several studies considered that afterslip is the dominant mechanism at short time scales (Hsu, 2006; Perfettini et al., 2010; Perfettini & Avouac, 2014), and it is generally modeled using the rate-and-state formalism, with afterslip occurring in a region with a velocity-strengthening friction regime. Within a steady-state approximation of the rate-and-state law (Dieterich, 1979; Marone et al., 1991), a logarithmic increase of slip with time is predicted from the rate-and-state formulation. This temporal evolution matches the aftershock decay rates, leading to the hypothesis that aftershocks are driven by afterslip (Perfettini & Avouac, 2004). However, the importance of viscoelastic relaxation in the first year of the deformation has been evidenced for the Tohoku-Oki earthquake by the landward motion recorded by offshore geodetic data, motion that can only be explained by viscoelastic deformation (Sun et al., 2014; Sun & Wang, 2015), and modeled using low transient viscosities in the mantle.

Previous studies investigating the early postseismic phase of large earthquakes are still quite rare, and include the M_w 6.4 2004 Parkfield earthquake (Langbein, 2006), the M_w 8.1 2003 Tokachi-Oki earthquake (Fukuda et al., 2009, 2013; Miyazaki & Larson, 2008), the M_w 7.2 2012 Nicoya earthquake (Malservisi et al., 2015), and more recently the M_w 7.8 2016 Pedernales earthquake (Tsang et al., 2019), the M_w 8.3 Illapel earthquake (Twardzik et al., 2021) and a compilation of studies including 4 megathrusts in South America (Twardzik et al., 2019). All these studies reveal the importance of early postseismic deformation, and the fact that measurements made using daily GNSS solutions can lead to a significant overestimation of the coseimic offsets. Concerning the mechanisms involved at this early stage, Langbein (2006) and Morikami & Mitsui (2020) show that the GPS data starting from a few minutes after the mainshock are adequately fitted by an « Omori-like » evolution of the velocity, *i.e.* $v \sim 1 / t^p$ and $p<1$. Fukuda et al. (2009) suggested that the Tokachi-Oki relaxation follows the prediction from the full rate-and-state formulation, including the acceleration phase (Perfettini & Ampuero, 2008). However, an alternative explanation for this apparent acceleration is the perturbation due to an early aftershock (Miyazaki & Larson, 2008).

We take advantage of the dense inland GPS network in Japan to investigate the postseismic deformation mechanisms after the great Tohoku-Oki earthquake which occurred on March 11, 2011 at 05:46:24 (UTC) near the northeast coast of Honshu. This earthquake has been widely recorded with various datasets, such as inland seismic and/or geodetic data, seafloor geodetic observations and tsunami data. Previous studies of the co-seismic phase feature a ~400 km (along strike) by ~150 km along dip slipping area, with a maximum slip that sometimes exceeds 50 meters at shallow depth close to the trench (see for a review Lay, 2018; Tajima et al., 2013; Wang et al., 2018). Previous works have been done on the postseismic phase of the Tohoku-Oki earthquake. Some only considered afterslip (Ozawa et al., 2012; Perfettini & Avouac, 2014) and revealed a large afterslip patch downdip from the co-seismic slip and possibly shallow afterslip (Perfettini & Avouac, 2014). Others also take into account the contribution from viscoelastic deformation (i.e. Sun et al., 2014; Sun & Wang, 2015). Two studies analyzed the early post-seismic phase of the Tohoku-Oki earthquake Munekane (2012), and Morikami & Mitsui (2020) using high-rate kinematic GPS data, revealing some details about the kinematics of the post-seismic phase, but without providing details on the possible mechanisms. In this study, we want to explore further the post-seismic phase of the Tohoku-Oki earthquake, more specifically at its early stages, and provide a mechanical interpretation about the observed evolution of deformation.

In this study, we characterize the temporal evolution of the postseismic deformation from minutes to years after the Tohoku-Oki event, combining 30-seconds kinematic GPS data for the early stages (from 10 minutes to 1 month) after the coseismic rupture and daily solutions for longer time scales (from 1 month to ~9 years). Then, we use simple analytical models to explain the temporal evolution of our data with the goal to constrain the mechanisms and the rheology of this postseismic phase. Following Montési (2004), we associate each temporal evolution to a given rheological model (afterslip, viscoelastic relaxation). Despite its simplicity, our approach aims at discussing the mechanisms at stake, and thus goes further than curve fitting approaches (Sobrero et al., 2020; Tobita, 2016) which only focus on finding the set of function minimizing the residuals.

Section 2 describes the GPS data used, processing methods employed to obtain the position time series, and the post-processing. In Section 3, we model the observed postseismic surface displacement using different rheological models. We show that afterslip with an "Omori-like" evolution of the velocity and an exponent of $p<1$ best fits our early postseismic data. We check how the model explains the observation at larger time-scales (~9 years) and we show that we should combine afterslip and viscoelastic relaxation. We discuss the physical meaning of the exponential decay and its implications for the fault rheology. In Section 4, we focus on the spatial pattern of postseismic slip by inverting the observed surface displacements to locate slip on the plate interface. We produce coseismic slip models for the mainshock and the largest M_w 7.7 Ibaraki-Oki aftershock which occurred ~30 minutes after the mainshock. Then, different time windows of increasing length are used to investigate the spatio-temporal evolution of the postseismic slip. Both analysis in Section 3 and 4 allow us to determine two separate types of behaviors. The first concerns regions which are directly affected by the Tohoku-Oki event, the other is a small region near the Ibaraki-Oki rupture area. In Section 5, we discuss the observed results, in particular the significance of the exponent $p<1$ found in our temporal evolution, in the light of results coming from numerical mechanic modelling.

2 GPS Data Analysis

The *GPS Earth Observation Network* (GEONET) network in Japan consists in around 1200 permanent GPS stations. In this study, we selected the 318 stations within a distance of 500 km from the Tohoku-Oki epicenter, which correspond to the stations that recorded the Tohoku-Oki mainshock, its main aftershocks (Figure 1a-b) and the postseismic signal (Nishimura et al., 2011).

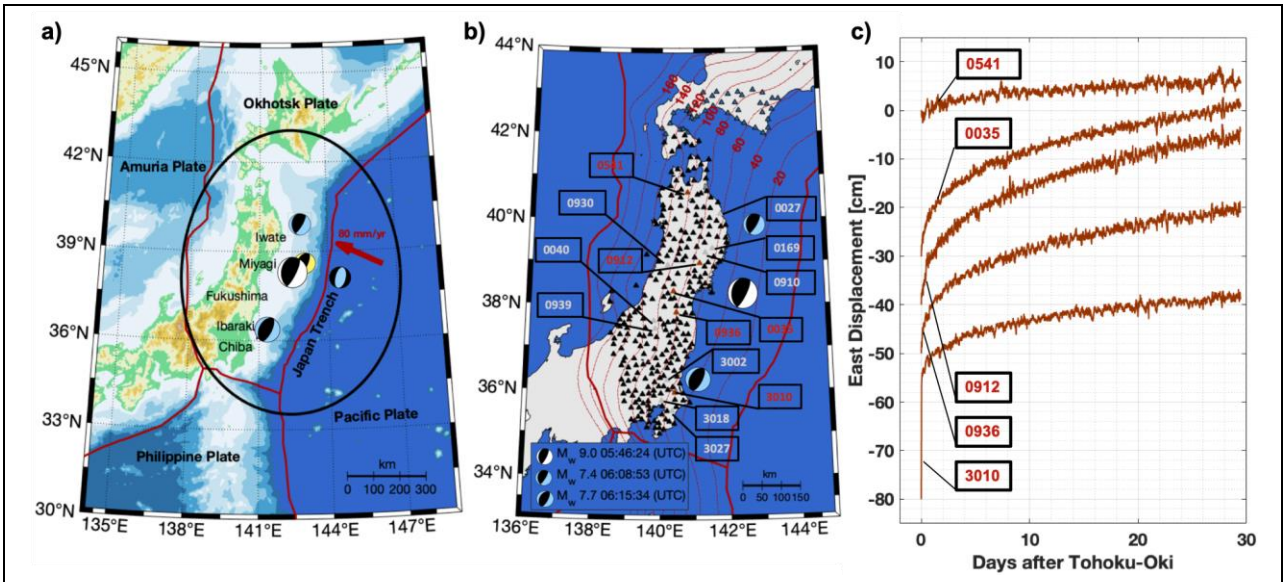

Figure 1 | Maps of the Japan Area and examples of GPS kinematic time series. a. Plate boundaries are illustrated in red, the associated Pacific interseismic loading (~80 mm/yr) is

represented with the red arrow. Significant earthquake focal mechanisms (F-net catalogue) sorted by size (yellow as foreshock, black as mainshock, black and blue as largest aftershocks). Stations used for this study are located within the black circle (distance from the mainshock epicenter less than 500 km). **b.** Black triangles are stations used for this study, brown triangles illustrate stations shown on Figure 1c, grey triangles are stations represented on Figures 2, 3, 5 and 6 and blue triangles are stations used to build the stack for the common modes correction. Earthquakes recorded by our kinematic data are the mainshock as well as the Ibaraki-Oki and largest north aftershock. Plates boundaries (red lines) and isodepth of the fault are given (red thinny lines). **c.** Postseismic signal from five different stations (shown on Figure 1b) on East component after the kinematic processing and post-processing phases applied (Sidereal Filtering and Removing Common Modes).

Our study is a compilation of two distinct GPS processing strategy: i) the first month after the mainshock is processed with high-rate kinematic 30-seconds solutions to investigate in details the fast motion at the beginning of the postseismic phase, and ii) from one month to ~9 years after the mainshock the time series are extended with daily solutions from static processing. In each case, the time series are processed with the Precise Point Positioning (PPP) approach (Zumberge et al., 1997), using the GIPSYX-1.3 software developed by the Jet Propulsion Laboratory (JPL). This single receiver approach requires high accuracy on satellites clocks and orbits (Bertiger et al., 2010). We used the final JPL clock corrections and orbits http://www.igs.org/products defined in the IGS14 reference frame (Altamimi et al., 2016). Tropospheric delays and gradients are estimated (every 30-secondes) using VMF1 mapping functions (Boehm et al., 2006) and we consider high order ionospheric terms using the IRI-2012 model (Bilitza et al., 2014). Ocean-loading effects are corrected using the FES2014b model (Spiridonov & Vinogradova, 2020). An elevation mask of 7 degrees is used. Antenna and radome models are used to correct phase center variations on antennas.

For the high rate positions, our processing strategy is similar to the multi-step iterative method described by Twardzik et al., (2019). To reduce high frequency noise in the time series, a Kalman filter is used during the processing of the GPS data, and the associated randomwalk parameters are selected to be suitable for detecting slow processes over time scales of hours to days. Following (Twardzik et al., 2019), and consistently with Choi (2007), we used 9.0e-5 m/√s for the troposphere zenith random walk parameter and 3.0e-4 m/√s for the random walk parameter of the Kalman filter for the kinematic positioning. We process separately the data from one month before the earthquake up to the origin time of the earthquake, and from 10 minutes after the origin time ($t_0^* = t_0$ +10 minutes) to one month after the earthquake. We start the time series at t_0^* to avoid perturbation due to the passing of the seismic waves. This separated processing for the data before and after the earthquake prevents our estimation of the co-seismic offset to be biased by the temporal smoothing induced by the kinematic processing. The obtained kinematic position times series are still biased by multipath effects due to the reflected waves recorded by receivers and common modes due to mismodelling of satellites orbits. To correct multipath effects (see Figure S1a), we build a sidereal filter following Twardzik et al. (2019), using the signal data from 7 days in the period before the earthquake. We also correct the time series from common modes following the approach of Marquez-Azua & DeMets (2003), by stacking signals (see Figure S1b) on stations far from coseismic and postseismic effects (blue triangles locations on Figure 1b).

We estimate the mean position uncertainty for each individual station and component by calculating the RMS over a period spanning one month before the foreshock (09/02/2011-09/03/2011). To quantify the improvement in time series quality associated with our post-processing, we estimated the RMS on each component, and we average over all stations. Our corrections lead to a global RMS reduction from 9.1 to 6.3 mm and from 9.5 to 7.0 mm on the North and East components respectively. The RMS reduction on the Vertical component is low (from 22 to 21 mm); this is expected as the Vertical component is highly sensitive to local uncertainties especially in the evaluation of the wet tropospheric delay. This, combined with a low postseismic signal on this component, implies poor signal to noise ratio on the Vertical. Consequently, we did not include vertical time series in the temporal subsequent analysis.

To summarize, our dataset consists of 30-s kinematic time series starting from 10 minutes after the earthquake origin time (t_0^* : 05:56:00 UTC) and up to 1 month after Tohoku-Oki, which we complete with daily solutions up to ~9 years after the mainshock. Among the 318 stations processed, five examples of final kinematic position time series are shown on Figure 1.c, with their locations indicated as brown triangles on Figure 1.b. For all the data (kinematic and daily static processing), we detrend the time series by removing the interseismic velocity, in order to focus on the postseismic signal only. The interseismic trend was estimated using a trajectory model (Marill et al., 2021), over a two years period (2009-2011) prior the earthquake (see Figure S2). Even if we start 10 minutes after the earthquake origin time, we were able to capture the co-seismic displacements of two large aftershocks. The first aftershock is a M_w 7.4 (06:08:53 UTC) located north of the mainshock, and we find some sites along the Miyagi-Iwate coast showing a coseismic displacement of a few centimeters. The second is the M_w 7.7 Ibaraki-Oki (06:15:34 UTC) earthquake, south of the mainshock (Figure 1a-b). Stations near the largest aftershock location, as station 3010 on the Figure 1c, show a well detected coseismic offset, partially smoothed by the Kalman Filter during the GNSS processing. We estimate the offsets due to the aftershocks using a time window from 9 to 27 minutes after t_0^* which allows to account for the smoothed offsets. This estimated coseismic offset is then removed from the postseismic time series which we analyze.

3 Modelling Postseismic Temporal Evolution

To model the postseismic temporal evolution, we firstly explore the characteristics of the temporal evolution of the surface displacements during the early stage of the postseismic phase, defined as the first month following the Tohoku-Oki earthquake. Then, using our daily solutions, we extended this analysis to a longer timescale of ~9 years.

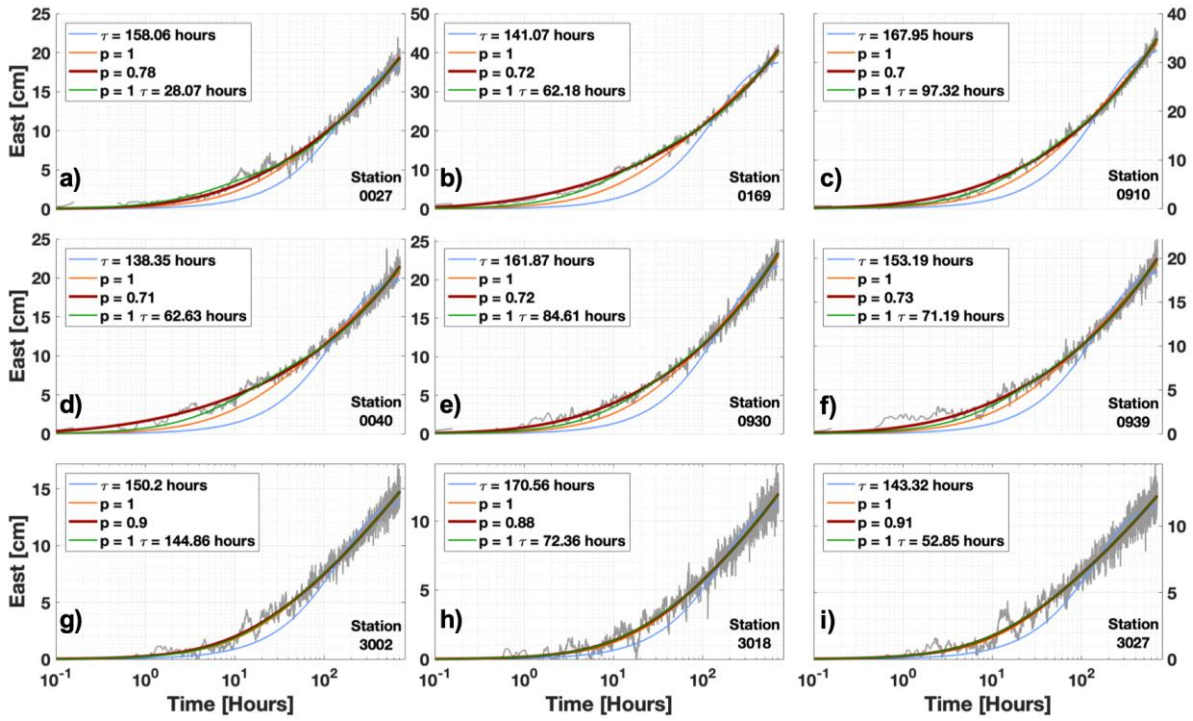

Figure 2 | Temporal Evolution and models used to fit GPS kinematic time series. a-i. Displacement evolution on the East component (grey curve) during the first month after the mainshock in logarithmic scale on the x-axis. Different mechanisms and models are tested, the mantellic viscoelasticity with an exponential velocity decay (equation **(2)** or **(4)** - blue curves), the velocity-strengthening afterslip associated to a logarithmic increase of the displacement (equation **(7)** - orange curves), the transient brittle creep mechanism described by an "Omori-like" signature characterized by a *p*-value (equation **(10)** - red curves) and the combination of mantellic viscoelasticity and velocity-strengthening afterslip (equation **(11)** - green curves). Station locations are represented on Figure 1b (grey triangles) and situated **a-c.** Near the coast of Tohoku **d-f.** Center of Japan **g-i.** Near the coast of Ibaraki.

3.1 Early Postseismic Deformation

In what follows, we consider that the stresses resulting from the coseismic rupture induce a postseismic relaxation accommodated by viscoelasticity in the mantle, afterslip, or a combination of both. Coupling this with an elastic crust from a simple conceptual model (Rice & Tse, 1986) gives rise to different expressions for the time evolution of surface velocities and displacements. These expressions are then compared to our GPS time series to discuss the underlying mechanisms at play. Using non-linear least-squares inversion, we compute parameters and uncertainties of the different models on surface displacement time series. We invert parameters for the East and North component to adjust postseismic kinematic position time series. Results obtained on East and North components are consistent but we choose to represent only results obtained on the East component which has the largest deformation amplitude, due to the mainshock location and the thrust faulting mechanism. Figure 2 shows the East component from

surface displacements of GPS stations located near Tohoku (Figure 2.a-c), in the central Honshu (Figure 2.d-f) and close to the Ibaraki coast (Figure 2.g-i). The location of these stations is given on Figure 1.b (grey triangles). The data gap between 9 and 27 minutes after t_0^* results from the removal of the period because of the occurrence of the two largest aftershocks recorded. Hereafter, the different possible mechanisms of postseismic deformation and the associated models are described, with the related data fitting description (see Figure 2).

3.1.1 Viscoelastic Relaxation

The first possible mechanism for postseismic deformation is related to the viscoelasticity of the mantle, which is commonly modeled from a Burgers rheology represented by a combination of a Maxwell fluid of viscosity η_M and shear modulus G_M, and a Kelvin solid of viscosity η_K and shear modulus G_K (Sun et al., 2014; Sun & Wang, 2015; Wang et al., 2012). The Kelvin, $\tau_K = \frac{\eta_K}{G_K}$ and Maxwell $\tau_M = \frac{\eta_M}{G_M}$ characteristic timescales are usually defined with $\tau_K \ll \tau_M$. Consequently, the transient Kelvin component of the rheology is considered to be predominant at short timescales, while the Maxwell component dominates at long timescales. Thus, in an early postseismic regime, a viscoelastic mantle submitted to a constant stress σ should give rise to a velocity $v(t)$ of the form:

$$v(t) = e^{\frac{-t}{\tau_K}} \quad \textbf{(1)},$$

with the initial postseismic velocity $v_0 = v(t = 0)$. Consequently the surface displacement $u(t)$ is given by the relation:

$$u(t) = v_0\tau_K\,(1 - e^{\frac{-t}{\tau_K}}) \quad \textbf{(2)}.$$

A best-fitting attempt of our GPS kinematic time series with expression **(2)**, with τ_K and the prefactor v_0 as adjustable parameters, clearly fails to reproduce the observations (blue curves on Figure 2). At longer timescales, the Maxwell component would add, under a constant stress, a constant velocity term proportional to η_M, *i.e.* a displacement increasing linearly with time, which is not observed in our data. However, in this case, a Newtonian flow of the mantle would relax the stress induced by the coseismic rupture, leading to a feedback loop between a decreasing stress and a stress-dependent rheology. To take this into account, following many others (Helmstetter & Shaw, 2009; Marone et al., 1991; Montési, 2004), we can write:

$$\frac{d\sigma}{dt} = -k\big(v_i - v(t)\big) \quad \textbf{(3)},$$

where v_i is the interseismic velocity resulting from tectonic loading and k a stiffness parameter representing the elastic stiffness of the lithosphere. This interseismic velocity (~cm/year) is negligible compared to our recorded early postseismic velocities (~cm/hour to cm/day). In addition, the time series have been corrected from the interseismic trend (see Figure S2). As (Montési, 2004) mentioned, coupling expression **(3)** with a Newtonian creep (*i.e.* $v{\sim}\sigma$) within a layer of thickness H predicts an exponential decay of the velocity that mimics equation **(1)**, hence leading to an expression similar to **(2)** for the displacement as,

$$u(t) = v_0\tau_*\,(1 - e^{\frac{-t}{\tau_*}}) \quad \textbf{(4)},$$

with a characteristic timescale $\tau_* = kH\eta_M$ (Montési, 2004). Note that although expressions **(2)** and **(4)** are similar, they correspond to different physical mechanisms.

As detailed below, early (~month) Tohoku-Oki postseismic deformation is characterized by an absence of a common characteristic timescale, in qualitative agreement with previous observations for other earthquakes (Savage et al., 2005). This rules out a predominant role of viscoelastic relaxation of the mantle during the early stage of the postseismic phase. We will discuss in more details below its possible role at longer timescales (~years).

3.1.2 Velocity-Strengthening Afterslip

We now consider that the elastic stresses induced by the coseismic rupture are relaxed through afterslip along a "creeping" section of the fault. Following many others (Marone et al., 1991; Perfettini & Ampuero, 2008), we first assume a velocity-strengthening rate-and-state rheology for this creeping region. Assuming further a rapid evolution of the state variable, the steady-state regime of this rheology is given by:

$$v = v_* e^{\frac{\sigma-\sigma_*}{a-b}} \textbf{ (5)},$$

where σ_* is the stress supported by the fault for a reference velocity v_*while a and b are the classical rate-and-state parameters. Coupling this rheology with relation **(3)** and a negligible interseismic loading rate ($v_i \ll v$) leads to a velocity history of the form (Montési, 2004), (see the conceptual model on Figure S3):

$$v(t) = v_0 \frac{c}{t+c} \textbf{ (6)},$$

with c a time constant depending on the rate-and-state parameters and the stiffness k. This then leads to a logarithmic increase of the displacement:

$$u(t) = c v_0 \ln\left(1 + \frac{t}{c}\right) \textbf{ (7)}.$$

Note that, in these expressions, c does not represent a characteristic *time-decay* for the velocity (as $\tau_K$in **(1)**), but a small *time-delay* before it transitions towards a power law decrease of v while avoiding a singularity at t→0. Expression **(7)**, with c and v_0 as adjustable parameters, fits our GPS kinematic time series much better than expression **(2)** (orange curves on Figure 2). Still, it is shown on Figure 3 that the corresponding residuals are significantly larger than the RMS of the signal for a majority of the analyzed GPS stations, especially for the first ~forty hours of the signal. This suggests that a velocity-strengthening rate-and-state rheology at steady-state improperly models our observations. Nevertheless, we find a small region close to the Ibaraki-Oki aftershock location where the velocity-strengthening afterslip model seems to properly explain the surface displacement evolution (Figure 2-3.g-i).

The model fails to fit the very early stage (*i.e.*, the first ~40 hours); this could be explained by the fact that, at short timescales, the steady-state approximation of the rate-and-state formulation is incorrect (Helmstetter & Shaw, 2009). Releasing this approximation, Perfettini & Ampuero (2008) performed a numerical analysis of the dynamics of a velocity-strengthening fault patch following a stress perturbation, and revealed a brief transient acceleration that we do not detect in our data, followed by a very fast velocity decrease before reaching a $1/t$ decay reminiscent of expression **(6)**. This is also not compatible with our kinematic GPS observations that show instead a velocity decay slower than $1/t$ from the onset of postseismic deformation (see below).

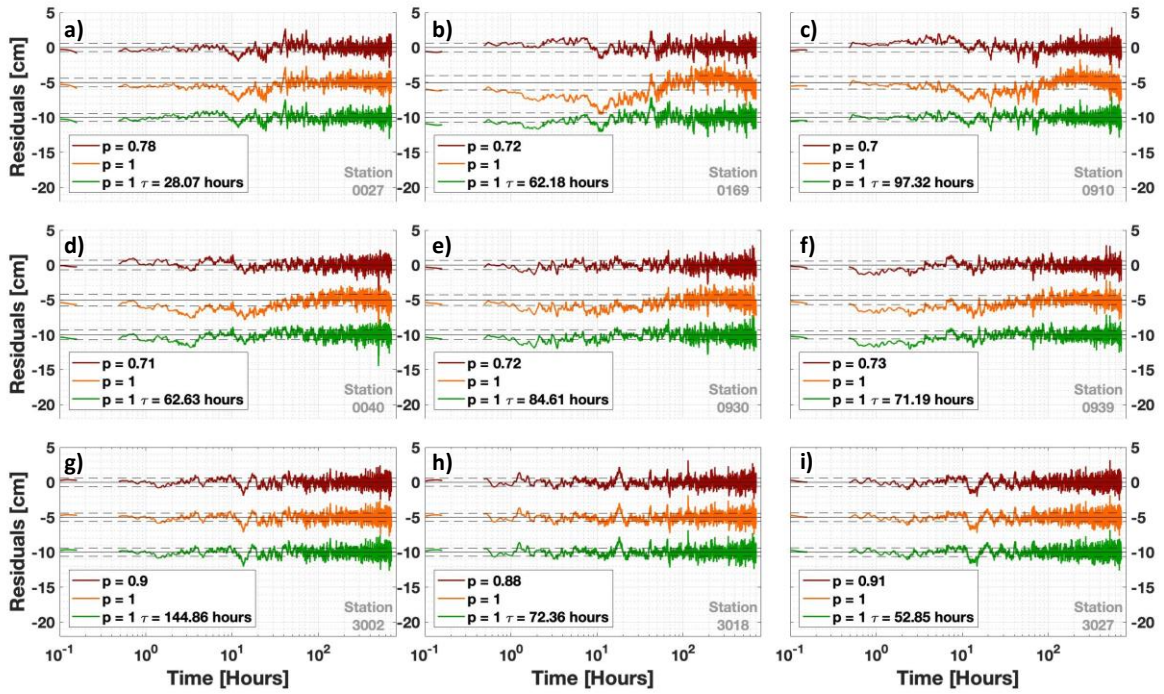

Figure 3 | Residuals Analysis. a-i. Residual displacements on the East component during the first month after the mainshock in logarithmic scale on the x-axis:
The transient brittle creep mechanism described by an "Omori-like" signature characterized by a *p*-value < *1* (equation **(10)** - red curves), the velocity-strengthening afterslip associated to a *1/t* decay of the velocity (equation **(7)** - orange curves) and the combination of mantellic viscoelasticity and velocity-strengthening afterslip (equation **(11)** - green curves). Station locations are represented on Figure 1b (grey triangles) and situated **a-c.** Near the coast of Tohoku **d-f.** Center of Japan **g-i.** Near the coast of Ibaraki.

3.1.3 Transient Brittle Creep

To explain the temporal evolution of postseismic surface displacements, some authors have invoked a transient creep mechanism within an unruptured section of the fault and its surroundings (Savage et al., 2005; Savage, 2007). Under constant stress, most of the materials exhibit initially a transient (primary) creep regime characterized by a decreasing strain-rate, before reaching a secondary creep regime of constant strain-rate. It has been observed empirically for a long time, including for rocks (Griggs, 1939) that this primary creep can be associated, depending on the material and the loading conditions, to a logarithmic increase of the strain, corresponding to a $1/t$ decay for the strain-rate. In our case, this would translate into expressions similar to equations **(6)** and **(7)** for surface velocities and displacements. Note however that the physical interpretation of such transient creep within a gouge and/or a damaged material surrounding the fault is different from a rate-and-state interfacial rheology discussed in the previous section. Scholz (1968), inspired by previous works on metals (Cottrell, 1952), proposed to explain this so-called transient logarithmic creep of rocks from the cumulative effect of numerous stress- and thermally-activated fracturing and local faulting events. We will come back later to the underlying hypotheses of Scholz's modelling. Here we just note that this

mechanism seems inconsistent with our early postseismic data, as we already stressed that equation **(7)** doesn't adequately fit our GPS kinematic position time series. However, such logarithmic creep appears as a special case rather than a common rule. Indeed, a more generic empirical expression of transient creep strain-rate $\dot{\varepsilon}$, including for rocks (Carter & Kirby, 1978) is:

$$\dot{\varepsilon} = A\sigma^n \left(\frac{c}{t+c}\right)^{-p} \exp\left(\frac{-E}{k_B T}\right) \textbf{(8)}.$$

Where $p \leq 1$, n generally lies in the range $2 \leq n \leq 4$ for rocks, A is a material constant, and the exponential term accounts for thermal activation characterized by E the activation energy (J), k_B the Boltzmann constant ($J.K^{-1}$) and T the temperature (K). In this framework, logarithmic creep corresponds to the end member where $p = 1$. Historically, Andrade (1910) was the first to report such power law decay of the strain-rate with p-values lower than 1 for metal wires with $p \approx 2/3$, which was later called Andrade's creep law. Translating this in terms of postseismic velocities,

$$v(t) = v_0(\sigma)\left(\frac{c}{t+c}\right)^{-p} \textbf{(9a)},$$

with the stress dependence expressed as,

$$v_0(\sigma) = A\sigma^n \textbf{(9b)}.$$

It leads to the following expression for the displacement:

$$u(t) = \frac{v_0 c}{1-p}\left[\left(1+\frac{t}{c}\right)^{1-p} - 1\right] \textbf{(10)}.$$

We fit our GPS kinematic time series with this last expression, with c, p and v_0 as adjustable parameters, and find on Figure 2 an excellent agreement with our data (red curves) for the first ~forty hours of the deformation signal. The corresponding residuals shown on Figure 3 (red curves) are almost flat and remain within the confidence interval determined by the signal RMS. We create a catalog of parameters and uncertainties obtained from the non-linear least square inversion. We use the parameter uncertainties to remove from the catalog stations with a poor signal to noise ratio (those far from the Tohoku-Oki earthquake) or stations with too many data missing, leaving 203 stations with a reliable estimate of p. Figure 4a shows the spatial pattern of the p exponent with its statistical distribution on Figure 4b. These figures indicate that most of p exponents are centered around 0.75. An exception is a small region close to the location of the Ibaraki-Oki aftershock location where p-values closer to 1 are observed. This observation is consistent with that made by Morikami & Mitsui (2020) who fitted velocities instead of displacements with expression **(9a)**. Our results, obtained directly from the fit of the displacement time series, are more robust as they do not depend on the time-binning chosen to estimate velocities. The vast majority of the delay times c are of the order of a few hours, without a clear spatial pattern (see on Figure 4c-d). Figure 4e indicates that the initial velocity v_0 is higher on the Tohoku coast (~4-5 cm/hr), and lower far from mainshock influence (~<1 cm/hr), consistently with a reduced influence of the coseismic stress perturbation. Stations along the Ibaraki coast are also associated to relatively large initial velocities (~<3cm/hr). Interestingly, p-values obtained for most of the stations are relatively close to the classical Andrade's exponent $p=2/3$. Overall, these results suggest that early postseismic deformation following the Tohoku-Oki earthquake could be explained by "afterslip" associated to a transient brittle creep mechanism within the gouge and the surrounding material. We will discuss in more details below the physical interpretation of this transient creep, in particular the signification of the p-value exponent.

In what precedes, we only considered a transient creep rheology under constant stress, *i.e.* without considering the stress relaxation induced by the deformation. If we now account for stress relaxation, by coupling this creep rheology (equations **(9a)** and **(9b)**) with expression **(3)**, it

can be shown that the resulting velocity history is unchanged at small timescales (t→0) whatever the *p*-value (expression **(9a)**), while at large time scales (t→ ∞), an apparent 1/*t* decay (*i.e., p=1*) is obtained. In particular, the logarithmic creep behavior (corresponding to equations **(6)** and **(7)**) remains phenomenologically unchanged. In other words, a $p<1$ value cannot be explained by stress relaxation, whose sole effect is to reinforce the velocity decay, *i.e.* to increase the apparent *p*-value. In our case, this suggests that the postseismic deformation during the first month after the coseismic rupture only marginally relaxed the induced stresses.

3.1.4 Combination of Viscoelastic Relaxation and Afterslip

To complete this analysis, we also considered a mixed model, combining a viscoelastic mechanism as described by equation **(2)** or **(4)** with afterslip along a "creeping" section of the fault associated to a logarithmic increase of the surface displacements (expression **(7)**). As we already described in the previous sections, this 1/*t* decay could be related to a velocity-strengthening rate-and-state rheology, (expressions **(5)**, **(6)** and **(7)**) or to the cumulative effect of numerous stress and thermally-activated fracturing and faulting local events (equation **(8)** with the particular case *p=1*),

$$u(t) = v_0 c\, ln\left(1+\frac{t}{c}\right) + v_1\tau_K\,(1-e^{\frac{-t}{\tau_K}}) \quad \textbf{(11)}.$$

This last tested model (green curves on Figures 2-3) is able to properly fit our GPS kinematic time series, including the first ~forty hours, better than the logarithmic decay model alone (equation **(7)**). The RMS computed on the residual's analysis of equation **(11)** (Figure 3) is similar to the value obtained for the transient brittle creep equation **(10)**. However, we rejected this model for two reasons. First, the obtained relaxation times τ_K or τ_* (**(2)** or **(4)**) for this combined model are very short, of the order of a few days. Using a Young's modulus of G_K= 50 GPa, this would imply Kelvin viscosities of the mantle η_K to be of the order of 10^{16} Pa.s, *i.e.* about 50 times smaller than commonly considered values (Wang et al., 2012). In addition, a conceptual model involving a single mechanism is always preferable to a more complex one combining different mechanisms.

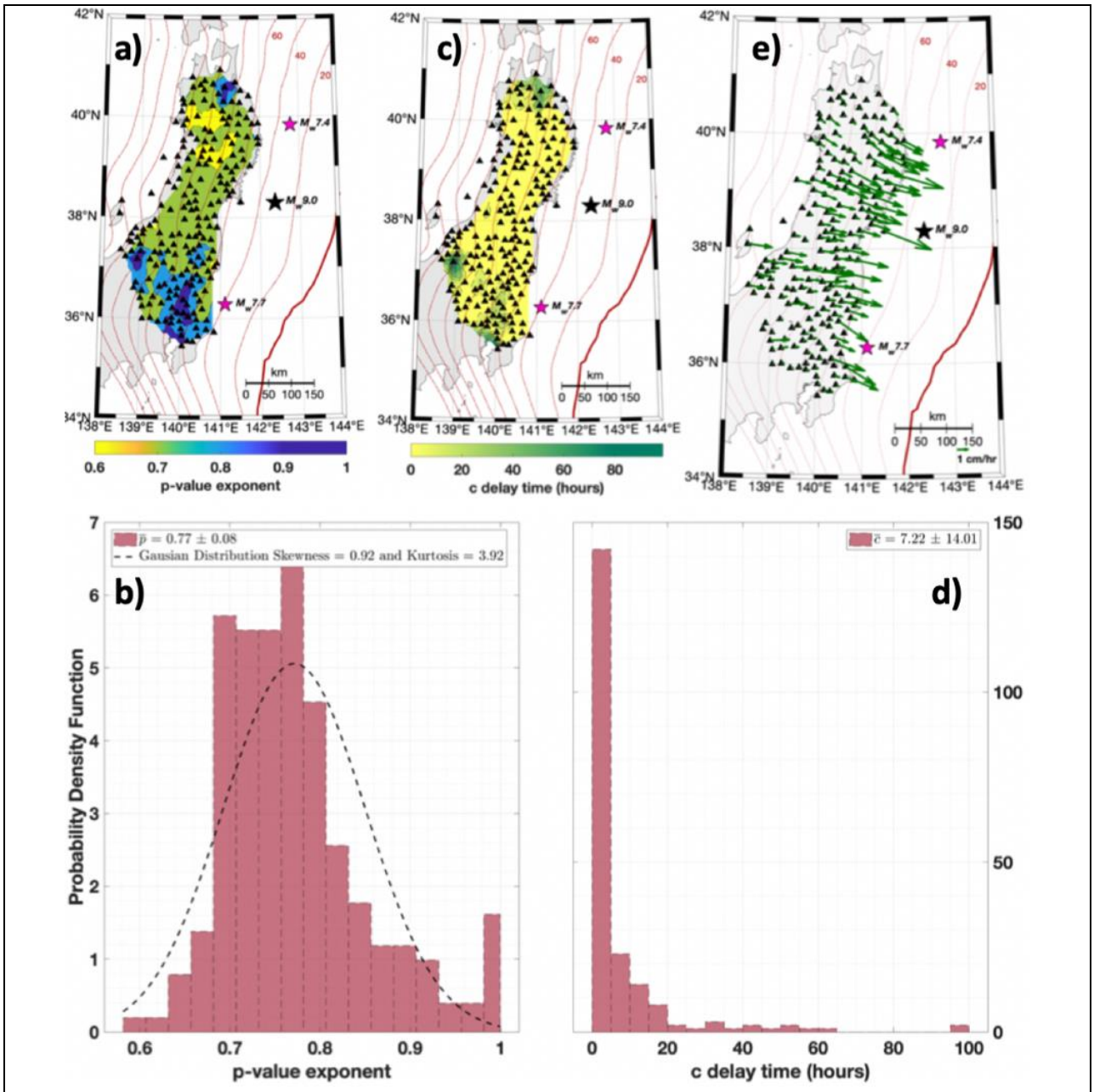

Figure 4 | Parameters and statistics obtained on 203 stations successfully inverted for time series up to 1 month: *p*-value exponents **a.** Interpolated map and **b.** Statistics and distribution. Time delay *c* in hours **c.** Interpolated map and **d.** Statistics. **e.** Map of horizontal initial velocity v_0.

3.2 Postseismic Deformation at larger time-scales

We have shown above that a transient brittle creep model with $p<1$ fits very well our early postseismic data, from a few minutes to one month after the mainshock. The following question is to determine to what extent such model can adequately explain postseismic deformation over longer timescales. To check this, we used position time series combining our kinematic (30-s) first-month time series with daily solutions extending up to ~9 years after the mainshock. At each station, the Omori-like decay (equation **(10)** for displacements) over this longer period shows a detectable deviation starting ~100 days after the Tohoku-Oki earthquake (Figure 5). This indicates that a transient brittle creep mechanism along the fault cannot account alone for postseismic deformation at timescales from several months to several years. On Figure 5, we show that an exponential (equation **(4)**) adequately fits the residuals of this transient creep model. This suggests a signature of a viscoelastic deformation of the mantle. Thus, we build a model that combine a transient brittle creep and a viscoelastic deformation of the mantle:

$$u(t) = \frac{v_0 c}{1-p}\left[(1+\frac{t}{c})^{1-p} - 1\right] + v_1\tau_*\,(1 - e^{\frac{-t}{\tau_*}}) \quad \textbf{(11)}.$$

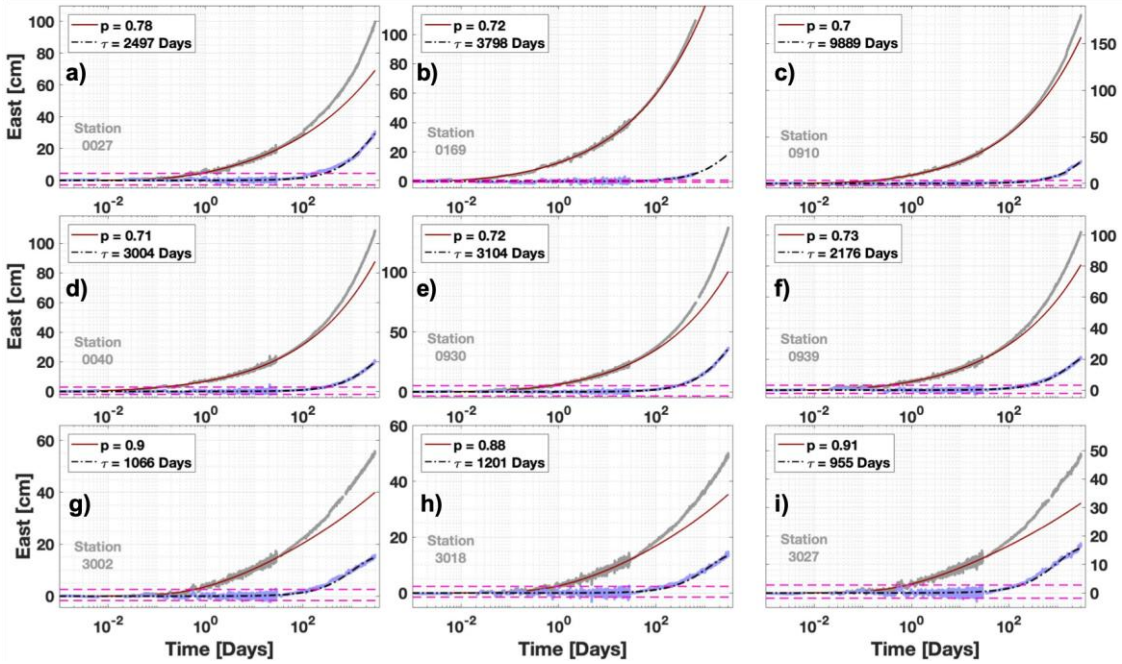

Figure 5 | Residuals Analysis of transient brittle creep model on the combination of GPS kinematic (over one month), + static time series up to ~2020. a-i. Displacement evolution on the East component (grey curve) during ~9 years after the mainshock in logarithmic scale on the x-axis. The *p*-value of the transient brittle creep (equation **(10)** - red curves) was determined over the first month. Then, the related residuals displacements are computed (blue curves) over large timescales.
The black dashed-dotted curves correspond to equation **(2)** or **(4)**. RMS of residual displacements is shown (magenta dotted lines). Stations locations are represented on **Figure 1b**

(grey triangles) and situated **a-c.** Near the coast of Tohoku **d-f.** Center of Japan **g-i.** Near the coast of Ibaraki.

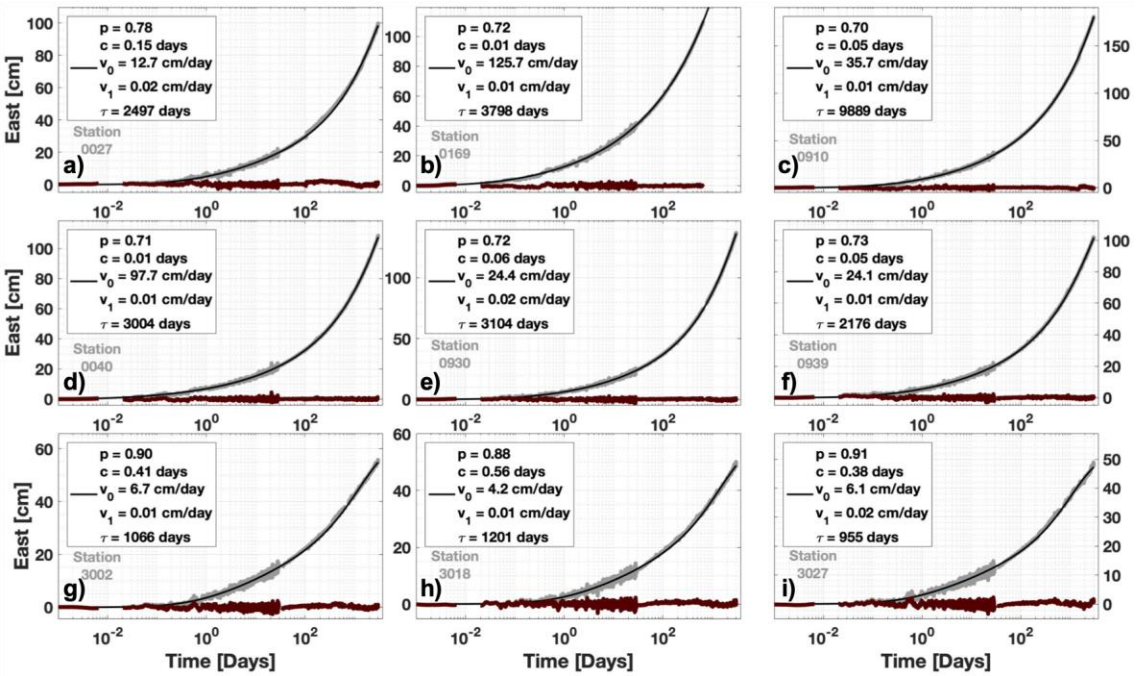

Figure 6 | Temporal Evolution and models used to fit GPS kinematic + static time series up to ~2020. a-i. Displacement evolution on the East component (grey) during ~9 years after the mainshock in logarithmic scale on the x-axis. The transient brittle creep mechanism determined by a *p*-value is combined with an exponential decay function associated to a mantellic viscoelastic mechanism (equation **(2)** or **(4)**) which the nature is debated in the discussion (black curves). Final residual displacements (brown curves). Station locations are represented on Figure 1b (grey triangles) and situated **a-c.** Near the coast of Tohoku **d-f.** Center of Japan **g-i.** Near the coast of Ibaraki.

Figure 6 shows how well this model explains our data from 10 minutes after the mainshock up to several years after. Here v_0, c and p have been obtained from our kinematic time series over the first month (section 3.1.3), while v_1 and the characteristic time τ_* have been determined from a similar non-linear least square inversion method on the residuals shown on Figure 5 (blue curves). Results are shown on Figure 6 (black curves). We explored the spatial variations on the relaxation time τ_* (see Figure 7a) and we observed a relaxation time around 7 years (statistics on Figure 7b), and which seems to be larger near the Tohoku-Oki earthquake. We have also explored the spatial variations of v_1 on Figure 7c and we find velocities v_1 of a few cm/year, which is orders of magnitude lower than the few cm/hr of the initial postseismic velocities v_0 obtained for the afterslip component. Considering a negligible stress relaxation and a shear modulus of $G_K = 50$ GPa, a characteristic timescale of ~7 years would yield a viscosity around 10^{19} Pa.s where the spatial variations of η_* are available on Figure S4. This is compatible with the values of the Maxwell viscosity reported in the literature (Sun et al., 2014).

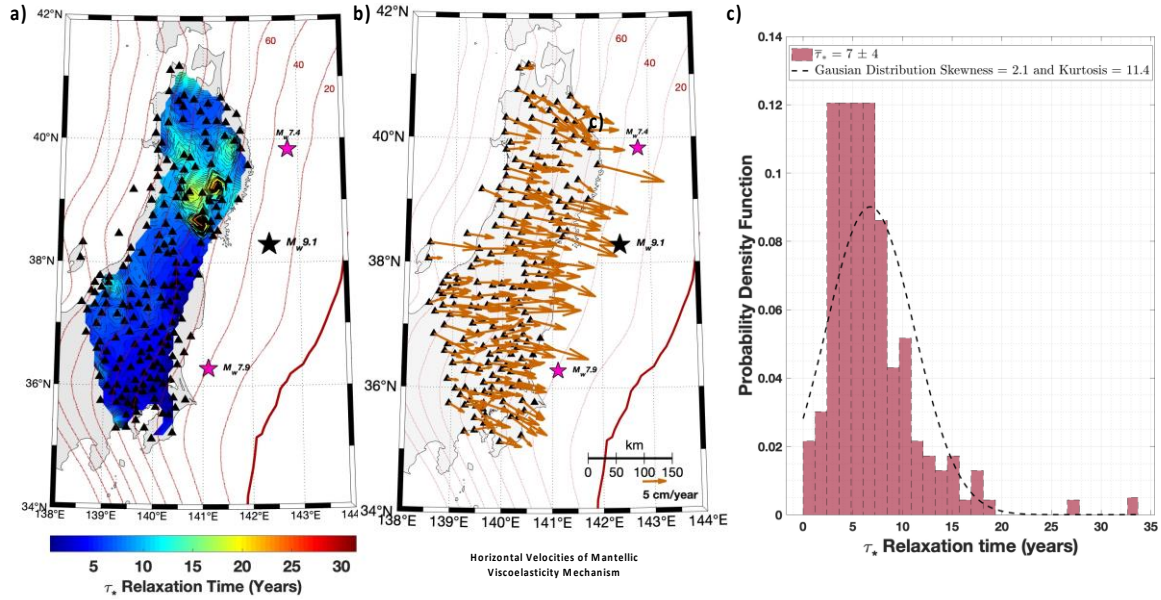

Figure 7 | Parameters and Statistics obtained on 192 stations successfully inverted for Time Series up to ~2020. a. Relaxation time τ_* interpolated map. **b.** Map of horizontal velocities v_1 associated to a mantellic viscoelastic mechanism. **c.** Relaxation time τ_* statistics and distribution

To conclude on the temporal evolution of the postseismic surface displacements after the Tohoku-Oki earthquake, we observe that the kinematic position time series during the first month following the earthquake are well explained with a transient brittle creep model, with a *p* exponent of about 0.75 on most of the region and a *p* exponent closer to 1 on the south nearby the Ibaraki-Oki aftershock. This temporal evolution differs from the *1/t* decay (*i.e. p=1*) predicted by velocity-strengthening friction. Over longer time scales (several years), an additional mechanism, compatible with viscoelastic mantle relaxation has to be considered. In the following, we investigate in more details the first month of the postseismic phase, and focus on its spatial pattern. In addition to the spatial variability in the *p*-value already discussed, we will estimate the location of the aseismic slip on the plate interface.

4 Static Inversion to constrain coseismic and postseismic slip

In what follows, we consider that the postseismic signal occurring during the first month after the earthquake is due either to frictional sliding on the plate interface or shear on a localized band around the interface, and we estimate its spatial distribution by inverting the GPS data (see details Text S1). We invert East and North components as well as Vertical component even if it is associated to larger uncertainties. In Japan, the large number of inland stations allows to estimate with a good spatial resolution the occurrence of slip below the island. However, the resolution is poor in the offshore region of the plate interface (see Text S2 and Figure S5). Using the configuration detailed in Figure S6a-b we estimate the slip on the plate interface by doing static inversions for 12 successive time windows.

4.1 Time windows definition

We estimate the postseismic displacements over the first month for several time windows with increasing duration, and select the time windows so that they correspond to a similar increase in surface displacement. We use the station 0930 as a reference, since it records among the largest postseismic displacements. The cumulative displacement windows $\Delta d = 2, 4, 6, \ldots$ cm define time windows $[t_0^*, t_0^* + \Delta t]$ of increasing duration from 3.25 hours to 29.4 days, see details in Figure S7. We end up separating the first month of postseismic record into 12-time windows, each corresponding to an almost identical amplitude of displacement, as shown in Figure S7. As the postseismic velocity decreases with time, the successive time-windows have an increasing duration. Then, we perform static inversions for the co-seismic displacements of the Tohoku-Oki and Ibaraki-Oki events, as well as for the cumulative post-seismic displacement over these different time windows.

4.2 Slip inversion procedure

For each time window considered, the horizontal and vertical displacements are inverted to estimate the slip on the subduction interface. We inverted East and North components as well as the Vertical component associated to large uncertainties (computed on time series in Section 2). We use the 3D geometry from Slab 2.0 (Hayes et al., 2018) to represent the Japanese subduction interface. The slab extends about 600 km along strike and 350 km along dip, down to a depth of 110 km. It is discretized in 1526 triangular patches of ~193 km^2. The static Greens functions are computed for an elastic half space using (Okada, 1992). We use a regularized least square inversion scheme following (Radiguet et al., 2011, 2016) (see details in Text S1). The selection of the optimal slip directions and regularization parameters is detailed in the Figure S6a-b.

4.3 Slip location for the mainshock, aftershocks and the early postseismic period

The slip models obtained for the mainshock and aftershocks coseismic displacements are shown on Figure 8a and 8b (see residual horizontal displacements Figure S8). The mainshock coseismic slip distribution has a moment magnitude of M_w 9.0 (assuming a Young Modulus E=50 GPa), and corresponds to a large area of shallow (<30 km) slip near the trench with a maximum amplitude of ~33 meters. This model, although constrained only by onshore GPS stations, gives a first order estimate of the co-seismic offset slip distribution for the Tohoku-Oki earthquake. Our model is consistent with several previously published models, but probably underestimates the large amount of slip close to the trench since we use only onshore GNSS data (see for a review (Lay, 2018; Tajima et al., 2013; Wang et al., 2018)). The inversion of the time window which includes the aftershocks, see below, (Figure 8b) [t_0^*+9 min – t_0^*+27 min] allows to estimate the slip distribution which corresponds to a magnitude of M_w 7.9. We identified a first slip region nearby the Ibaraki prefecture which is associated to the aftershock of Ibaraki-Oki (06:15:34 UTC) which has a magnitude of M_w 7.7 (F-NET) or M_w 7.9 (USGS). We also remarked a small slip dip area north of Tohoku-Oki which corresponds to the location of a M_w

7.4 (06:08:53 UTC) aftershock (identified by F-NET), that occurred during the same 18 minutes time window.

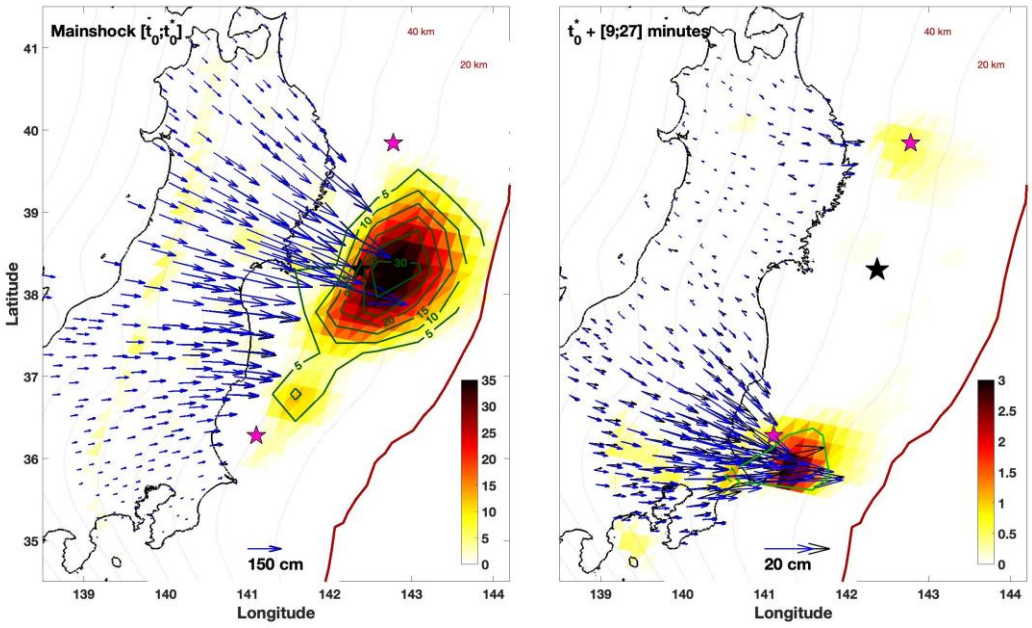

Figure 8 | Spatio-temporal evolution of a. Tohoku-Oki coseismic offset (05:46:00-05:56:00 UTC) with $\chi = 16.2$ **b.** Ibaraki-Oki coseismic offset (06:06:00-06:24:00 UTC) with $\chi^2 = 2.8$. Black and blue arrows represent observed and predicted horizontal displacements. Green lines represent slip contour in meters. Stars correspond to the epicenters of the three main events. Color scale indicates the slip amplitude in meters.

To explore the postseismic period, we remove the aftershocks coseismic offsets, estimated by a step function, from the time series. We represent the cumulative (since t_0^*) slip distribution during the first month of the postseismic period, for the 12-time windows of increasing duration (see Figure 9 and residual horizontal displacements Figure S9), as defined in Section 4.1. For the first snapshot (Figure 9a, t_0^* + 3.25 hours), the signal is slightly above the noise level (maximum 2 cm of displacement at some stations), and it is difficult to distinguish a clear pattern in the slip distribution, although the slipping area is located downdip the mainshock (a distribution that is potentially biased by the lack of resolution nearby the trench). The successive snapshots for the first day (Figure 9b-c) reveal a coherent trenchward motion of the GPS network. Our inversion reveals two main afterslip regions: one located just below the Tohoku-Oki co-seismic slip rupture, and a second one south of the Ibaraki-Oki aftershock, while between these 2 regions, an intermediate zone at the latitude ~37°N (see Figure 9d-l) do not show significant afterslip. The existence of these two well-separated patches of afterslip is actually visible in the pattern displayed by the surface GPS displacements, characterized by two groups of GPS stations pointing towards two distinct directions. The amount of postseismic surface displacements and corresponding afterslip for the first day after the event, shown in Figure 9 a-c is not available using daily GPS solution alone. We can see that this first day early afterslip is significant, with maximum horizontal displacements of 18 cm, corresponding to an equivalent magnitude of M_w 8 for the whole subduction interface (see Figure 10.a-b).

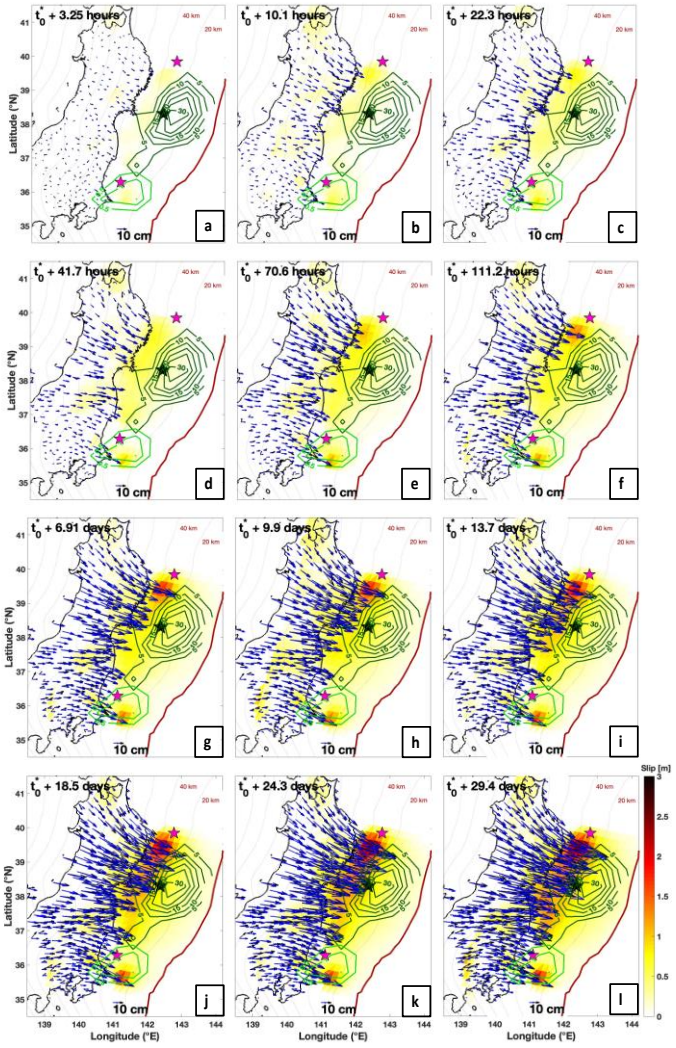

Figure 9 | Spatio-temporal evolution of afterslip during the first month on 12-time windows: Aftershock(s) coseismic offsets are removed from the postseismic deformation. Black and blue arrows represent observed and predicted horizontal displacements. Green lines represent slip contours of the Tohoku-Oki mainshock and Ibaraki-Oki aftershock in meters. Stars correspond to the three main events. Color scale indicates the slip amplitude in meters. **a.** $t_0^* + 3.25$ hours and $\chi^2 = 7.2$. **b.** $t_0^* + 10.1$ hours and $\chi^2 = 4.1$. **c.** $t_0^* + 22.3$ hours and $\chi^2 = 25.5$. **d.** $t_0^* + 41.7$ hours and $\chi^2 = 39.4$. **e.** $t_0^* + 70.6$ hours and $\chi^2 = 18.2$. **f.** $t_0^* + 111.2$ hours and $\chi^2 = 11.2$ **g.** $t_0^* + 6.91$ days and $\chi^2 = 54.0$. **h.** $t_0^* + 9.9$ days and $\chi^2 = 27.6$. **i.** $t_0^* + 13.7$ days and $\chi^2 = 41.1$. **j.** $t_0^* + 18.5$ days and $\chi^2 = 43.4$. **k.** $t_0^* + 24.3$ days and $\chi^2 = 73.8$. **l.** $t_0^* + 29.4$ days and $\chi^2 = 9.5$.

Our slip inversion shows that the largest amplitude of the early afterslip is located mostly at depth between 30 and 50 km, downdip of the coseismic slip, and is separated in two patches (region 1 and region 2 in Figure 10a), in agreement with previous studies (see for a review (Lay, 2018; Tajima et al., 2013; Wang et al., 2018)). Our inversion also shows some afterslip of lower amplitude propagating in the coseismic rupture zone. Given the low resolving power of our onshore GNSS data to offshore slip (see Text S2 and Figure S5), we consider that this feature is not well resolved. A robust pattern is the identification of two main afterslip regions, one located just below the mainshock and another one on the south, associated to the M_w 7.7 aftershock, separated by a region of low afterslip (Figure 10a). We postulate that these two regions could be associated with the different temporal evolutions identified in the previous section. We estimate the equivalent seismic moments and magnitudes released aseismically for these two regions (Figure 10b-c) and their associated moment rates (Figure 10d). As expected, region 1 (below the mainshock) has a larger magnitude than region 2 (M_w 8.1 versus M_w 7.4 after 1 month). Despite the low temporal resolution of our kinematic inversion (12 sequences over 1 month), a fit to the temporal evolution of the cumulative moment using equation **(10)** gives an optimal p value of 0.8 for region 1 and 0.99 for region 2, which is compatible with the models from in the previous section obtained using the position time series (with p~0.75 in region 1 and p~1 in region 2), and confirms the differences in the temporal evolution of afterslip for the two regions.

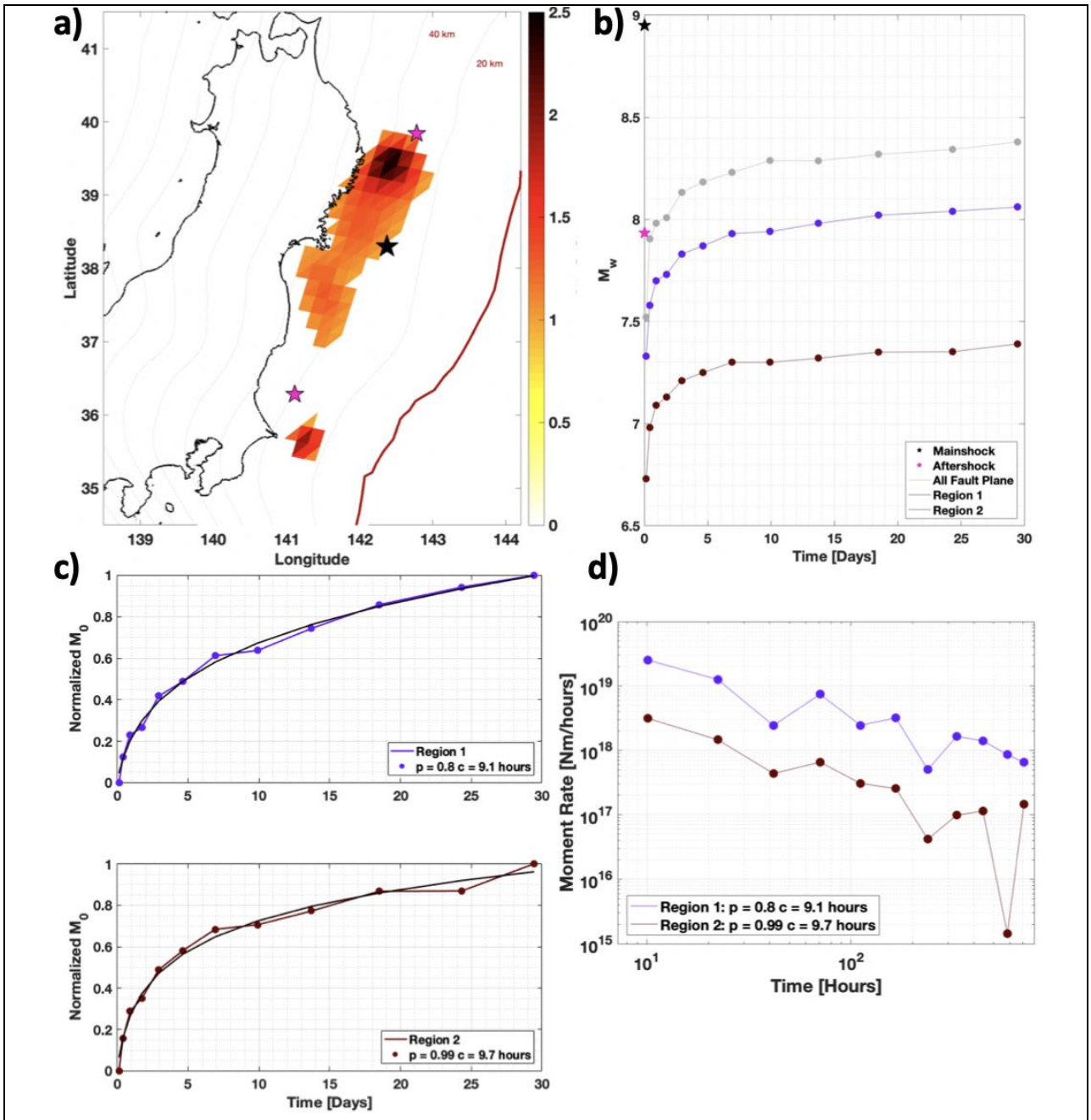

Figure 10 | a. Afterslip during the first month following Tohoku-Oki divided in two main areas: region 1 in the North (afterslip central and northern patch near the Iwate-Miyagi coast) and region 2 in the South (afterslip near Ibaraki coast) are defined by a slip larger than 1 meter. **b. Equivalent seismic magnitude** of the postseismic slip computed over time for all the fault plane (grey line), region 1 (blue line) and region 2 (brown line). Black and magenta stars represent the seismic magnitudes of the mainshock and the aftershock, respectively. **c. Equivalent seismic moment normalized** between 0 and 1 over time, black lines represent the best-fit following equation **(10)** for both regions. **d. Moment Rate** computed over the time window [t_0^* +10.1 hours and t_0^* +29.4 days].

5 Discussion

The former observations of early postseismic deformation following large subduction earthquakes were limited by the low number of GPS time series (Twardzik et al., 2019). The Tohoku-Oki earthquake studied in this paper represents an opportunity to improve our understanding of such postseismic phase and to constrain its temporal evolution over a wide range of timescales (Malservisi et al., 2015), owing to the large aseismic displacement recorded and the dense network of GPS stations. In Section 3, we argued that our GPS time series, from the timescale of a few minutes to that of several years after the coseismic rupture can be explained by a combination of afterslip, largely dominant at short timescales, and a viscoelastic relaxation process of the mantle at longer timescales. Hereafter we mainly discuss the nature of the afterslip mechanism, which dominates the early postseismic stage with an Omori-like signature (Figure 2). Its temporal evolution mostly depends on the *p*-value (equation **(10)**) which we found, consistently with (Morikami & Mitsui, 2020), to be significantly smaller than 1 except for a small region near the Ibaraki-Oki aftershock where the *p*-value is closer to 1 (Figure 4a). We have highlighted that this $p<1$ value is incompatible with a classical velocity-strengthening regime of a rate-and-state rheology. Hereafter we propose a possible mechanism to explain *p* values lower than 1, which we attempt to validate using numerical mechanical modelling.

5.1 Velocity-Strengthening interfacial rheology versus Transient Brittle Creep

As we already mentioned above, the current interpretations of afterslip are either based on a velocity-strengthening regime of a rate-and-state rheology for a frictional interface (Marone et al., 1991; Perfettini & Ampuero, 2008; Perfettini & Avouac, 2004), or a transient creep mechanism (Savage, 2007; Savage et al., 2005). Although these two interpretations appear at first glance as being different in nature, they actually share some similarities in their underlying physics. Scholz modeled transient brittle creep as resulting from the cumulative effect of numerous stress- and thermally-activated fracturing events, (Scholz, 1968) each of them inducing a small strain/slip increment, and predicted a logarithmic strain (or slip) of the type $\varepsilon(t)\sim\ln(1+\frac{t}{c})$, corresponding to a strain-rate (or slip velocity) decaying in $\frac{1}{t}$, *i.e.* $p=1$. In other words, this approach is unable to model the $p<1$ values characterizing the early phase of afterslip for the Tohoku earthquake in most regions (Figure 4.a). However, Scholz's model, reconsidered more recently by Savage and co-workers in the context of post-seismic deformation (Savage, 2007; Savage et al., 2005), is based on several strong simplifying assumptions:

(i) An exhaustion hypothesis, *i.e.* a local site/asperity cannot slip more than once
(ii) An absence of mechanical interactions between slip events

On the other hand, the rate-and-state rheology originates from an empirical formulation based on laboratory sliding-block experiments (Dieterich, 1979; Marone, 1998). (Baumberger et al., 1999; Heslot et al., 1994) considered the role of thermal activation of local slip events to explain the velocity-strengthening regime of dynamic friction, as well as the aging of the interface under constant normal stress (the state effect). This suggests a similarity with brittle creep. However,

much like in Scholz's model of brittle creep, they neglected elastic interactions between microslip events.
As we will show in Section 5.2, these simplifying assumptions are unphysical, and their release allows modeling a transient creep with *p*-values lower than 1, as well as possible effect of temperature on the *p*-value.

5.2 Transient Brittle Creep as a combination of thermally-activated processes and eslastic stress transfers

To explore this, we used a damage model, which takes into account elastic interactions, and implemented thermal activation from a kinetic Monte-Carlo algorithm (Bortz et al., 1975). The athermal version of this damage model has been thoroughly detailed elsewhere (Amitrano et al., 1999; Girard et al., 2010), hence we will only recall its main characteristics here. In this 2D model (see Figure 11), an elastic domain is discretized into N finite-elements, all with the same Young's modulus E_0. Loading is applied on the boundaries of the domain. Initial disorder is introduced from a spatially variable cohesion drawn from a uniform distribution. At the element scale, damage of the material, i.e a decrease of the modulus E by a factor 1-d (with d=0.1 for the simulations presented below), occurs whenever the local stress state reaches a Mohr-Coulomb's criterion (see Figure S10). This local softening generates a strain increment. After each damage event, the static equilibrium is re-calculated while the external loading is maintained constant, inducing a redistribution of elastic stresses within the domain, which can potentially trigger additional damage events, particularly in the vicinity of the former one (see details in Figure S10). This was shown to successfully reproduce the main characteristics of rocks damage and Coulombic failure, such as the progressive localization of damage upon approaching a peak stress at which an incipient fault nucleates, or the impact of confining pressure and of the internal friction μ on strength and on the mechanical behavior (ductile *vs* brittle) (Amitrano, 2003; Amitrano et al., 1999). This way, our model physically considers elastic interactions between damage/strain events, *i.e.* releases the assumption (ii) of Scholz's model mentioned above. In addition, a given element can damage several times in the course of deformation, hence releasing the exhaustion assumption (point (i) above). Such cascades of events eventually explain damage and strain localization along a "fault". There is no explicit timescale in the athermal version of the model, which is therefore unable to simulate creep deformation under a constant external loading. (Amitrano & Helmstetter, 2006) introduced time-dependent damage within this framework from deterministic static fatigue laws at the element scale. This allowed to successfully reproduce the phenomenology of creep of rocks, including the transition from stage I (a decelerating creep) to stage III (an accelerating creep) preceding failure.

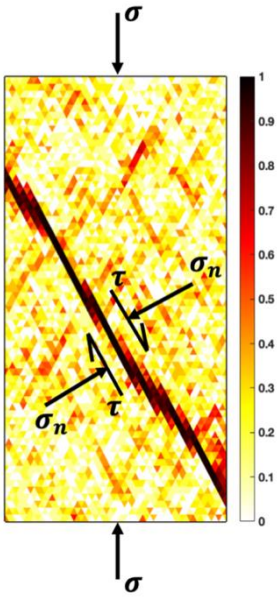

Figure 11 | Progressive damage modelling of transient brittle creep. The elastic domain is discretized into N-finite elements of initially equal Young's modulus E_0 but a variable cohesion. The figure represents the damage field obtained at the end of the athermal pre-loading stage, with an incipient inclined fault. The color represent the damage values, normalized such that the maximum damage values, *i.e.* the minimum elastic moduli, are shown in black along the fault. This faulted domain is then reloaded under a constant external uniaxial creep stress σ, with thermal activation switched on. This leads to a resolved shear stress τ along the fault plane and a normal stress σ_n.

We consider here a different approach based on a stochastic, physics-based modeling of thermal activation. In the athermal model, damage can only occur when the local stress state reaches the Mohr-Coulomb failure envelope. In this new version, at any time *t* a damage event can occur at element *I*, with a probability:

$$P_i \sim \exp\left(\frac{-E_a^i}{k_B T}\right) \textbf{ (12)},$$

where k_B=1.38 10^{-23} J.K^{-1} is the Boltzmann constant, T the temperature, and E_a^i an activation energy of damage for the element *i* in J. A natural choice for this activation energy is (Castellanos & Zaiser, 2018):

$$E_a^i = V_a \Delta\sigma_i \textbf{ (13)},$$

where V_a is a spatially constant activation volume and $\Delta\sigma_i$ a Coulomb stress gap between the stress state of the element *i* at time *t* and the Mohr-Coulomb failure envelope. The kinetic Monte-Carlo algorithm allows to randomly select in an efficient numerical way, following a probability P_i, the element *i* that will damage next after a Δt_i time delay. This is not necessarily the one which is the nearest from its local damage threshold, although its probability of damage is the largest **(12)**. As soon as a damage event is thermally activated, elastic stresses are redistributed without advancing further the time (the corresponding elastic timescales are considered to be negligible compared to those of thermally-activated creep), and possibly trigger new damage events in an athermal way. Once such an athermal cascade stops, a new thermally activated event

j is selected and time increases by Δt_j. This way, the model combines thermally-activated damage and deformation as well as elastic stress redistributions. In what follows, the values of V_a and T, as well as the distribution of local cohesion values have been chosen arbitrarily. Indeed, we are not interested in predicting quantitatively creep kinematics for some specific material, instead in simulating the phenomenology of transient creep.

To do this, we considered the following loading protocol (see details in Figure S10). The internal friction coefficient is fixed to μ=0.7. A rectangular domain is first compressed uniaxially under a monotonic and *athermal* way, following previous works (Amitrano et al., 1999; Girard et al., 2010). This leads to the development of an inclined fault of highly damaged material, associated to a large macroscopic stress drop. We stop this preliminary step just after this stress drop, and unload the domain. The resulting damage pattern then serves as an initial condition (see Figure S10) for a second step. During that second step the kinetic Monte-Carlo algorithm is switched on and the domain is re-loaded under a constant macroscopic uniaxial compression stress σ_0 (creep mode) corresponding to some % of the stress remaining after the stress drop of step 1. This way, we simulate the creep of a pre-damaged fault under both normal and shear stress components along the fault plane. In this configuration, all damage and deformation accumulating during the transient creep loading concentrates along the pre-existing fault, while the upper and lower blocks mimic the role of much stiffer elastic plates, however allowing elastic stress transfers. All the results summarized below have been average over 10 realizations of the initial disorder (see Figure 12).

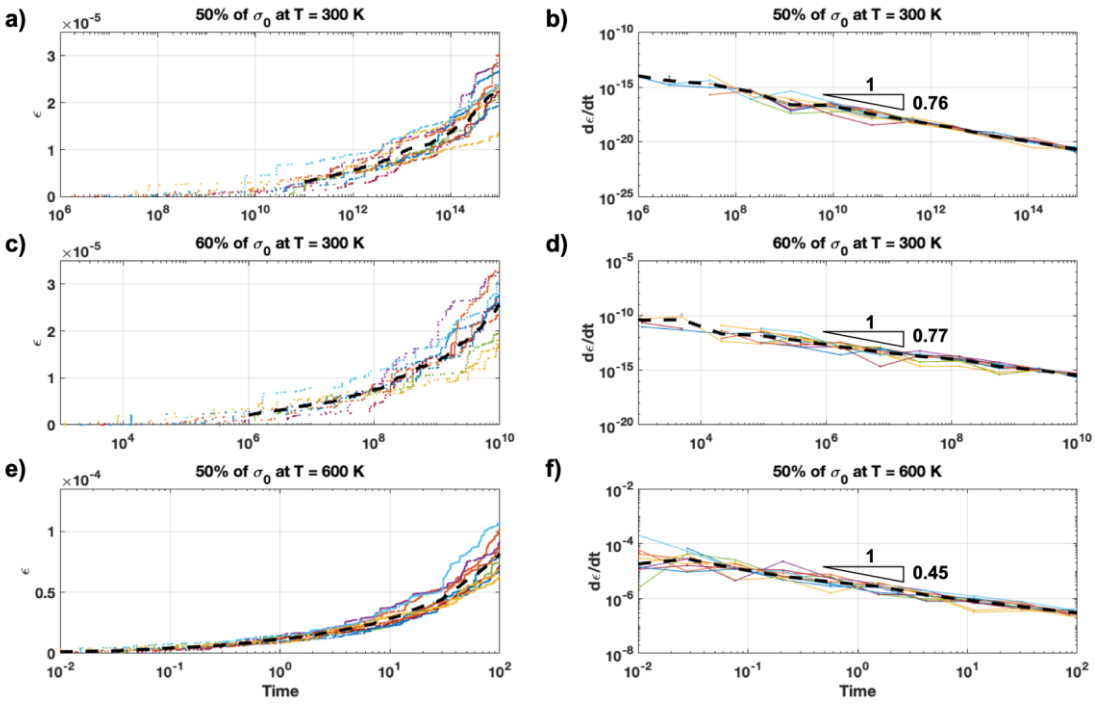

Figure 12 | Strain ε (left) and Strain Rate $\frac{d\varepsilon}{dt}$ (right) obtained for the creep deformation of the modelled domain, with the following modelling parameters: Friction coefficient μ = 0.7, constant loading maintained at 50% or 60% of the stress remaining after the stress drop of the

pre-loading stage, for T = 300 K **(a-d)** or T = 600 K **(e-f)**. Ten simulations corresponding to different realizations of the initial disorder were performed in each case, and the black dotted curves represent the average response where the slopes represent the *p*-values estimated. The present curves focus on the transient creep (stage I).

The resulting macroscopic strain $\varepsilon(t)$ and strain-rate $\dot{\varepsilon}(t)$, which can therefore be directly linked to a displacement and average "slip velocity" along the fault, follows the typical phenomenology of rocks creep with a decelerating primary (or transient) creep stage I (see Figure 12 b,d,f) followed by an accelerating stage III (see Figure S11). Note that, in our simulations and much like what is observed in rocks, the creep stage II associated to a supposedly constant strain-rate $\dot{\varepsilon}_{min}$ seems to manifest only in the form of an inflection point (see Figure S11). We are not interested here in the accelerating stage III, which resulted in our simulations from the development of a secondary conjugate fault, and focus instead on the transient stage I (see Figure 12 b,d,f) during which all deformation occurs along the pre-existing fault (see Figure S10). Note that under a slow constant strain-rate loading condition, more consistent with tectonic loading at large timescales, such accelerating creep (stage III) would not occur as the primary creep would relax the stress.

In our simulations, the transient creep (stage I) is characterized by a power-law decay of the strain-rate, $\dot{\varepsilon}(t) \sim 1/t^p$, with a *p*-value always smaller than 1, over several orders of timescales (Figure 12). We can therefore conclude that a transient brittle creep mechanism combining the thermal activation of damage/strain/slip events as well as elastic stress interactions allows reproducing the phenomenology of Tohoku early afterslip. This can be qualitatively interpreted as follows: a *p*-value smaller than 1 implies a slower decay of the afterslip rate compared to p=1. This comes from the fact that, unlike for the simpler Scholz's approach, a thermally activated event can trigger a cascade of athermal events, or the associated stress redistribution can advance the clock of thermal activation of other sites, in the end sustaining the creep dynamics. In addition, a given site/asperity can slip several times during afterslip, while Scholz excluded this possibility with his exhaustion assumption.

By increasing the applied creep stress while keeping the temperature T unchanged (see Figure 12 a-b), we observed a shortening of the transient creep stage I (see Figure S11), as expected, but no significant modification of the *p*-value. Instead, an increase of temperature T, while keeping the applied stress constant, appears to decrease the *p*-value as observed for rocks creep in laboratory tests (Carter & Kirby, 1978), see Figure 12 a-c.

5.3 Identification of two main Afterslip regions

The detailed inversion procedure provides a robust pattern which allow the identification of two main afterlip regions (Figure 9 and 10a), one below the mainshock and another one, separated by a zone of lower afterslip, located on the south. This spatial separation (Figure 10) and the analysis of the temporal evolution of afterslip on the northern and southern region (Figure 2, 4 and 10b), have shown a different behavior defined by a larger *p*-value on the southern region. The postseismic deformation recorded in the Southern region is most likely the consequence of the M_w 7.7 Ibaraki-Oki earthquake, this large aftershock having triggered its own afterslip sequence which can be detected by the nearby stations. One possible explanation to understand why afterslip in this region 2 evolves differently with respect to the region 1 could be related to a

862 temperature effect. In the southern region, thermal models (Ji et al., 2016) suggest a negative
863 thermal anomaly, related with the nearby subduction Philippine sea plate. The results of our
864 numerical simulations (Figure 12) provide some clues that a lower temperature could have some
865 impact on the transient brittle creep signature (*i.e.*, higher *p*-values). This could potentially
866 explain, at least partly, the larger *p*-values observed south of 37°N (see Figure 4a).
867

868 5.4 Postseismic deformation at larger timescales and Viscoelastic Relaxation

869

870 At timescales larger than a few months, transient afterslip is unable to fully explain our
871 displacement records. We have shown that the associated residuals are characterized by an
872 exponential decay (figures 5-6), therefore suggesting a combination of transient afterslip and
873 viscoelastic relaxation in the mantle (see equations **(2)** and **(4)**) to explain the entire postseismic
874 deformation from a few minutes after the coseismic rupture up to several years.
875 As mentioned in Section 3, considering a classical Burgers rheology for the viscoelasticity of the
876 mantle with two characteristic timescales $\tau_K \ll \tau_M$, such an exponential decay can be explained
877 either by (i) a transient viscoelasticity regime (associated to τ_K) under a constant stress (equation
878 **(2)**), or (ii) the Maxwell component of the rheology (associated to τ_M) relaxing the stress
879 (equation **(4)**). The viscosities obtained from our data, around 10^{19} Pa.s, are in favor of the
880 second explanation.
881 Our analysis did not include the near-trench observations coming from seafloor GPS
882 measurements, as the first data obtained contain several days of postseismic signal. This is the
883 major difference with the studies of (Sun et al., 2014; Sun & Wang, 2015). These authors
884 observed a landward motion of the zone nearby, in opposition with the seaward motions
885 recorded by the land GPS stations. Considering this near-field observations, they modeled the
886 postseismic deformation with a transient viscoelastic mantle rheology in the oceanic mantle.
887 They argued that a non-negligible role of this viscoelasticity leads to a large reduction of the
888 afterslip required to explain the land GPS data. However, their conclusion is not necessarily in
889 contradiction with ours, as the period covered by their study is 1 to 3 years after the Tohoku-Oki
890 earthquake, while we show that afterslip associated to a transient creep mechanism dominates the
891 postseismic deformation up to few months after the coseismic rupture. Over this early period, we
892 consider viscoelastic relaxation of the mantle to be negligible to explain the motions of the GPS
893 stations installed in mainland Japan.
894

895 **6 Conclusions**

896

897 We processed and analyzed high-rate (30-s) GPS solutions recorded during the first month after
898 the M_w 9.0 Tohoku-Oki megathrust earthquake (2011), and complemented this dataset with daily
899 solutions at larger timescales, up to ~9 years after the mainshock. This allowed us to explore the
900 kinematics of postseismic deformation following a megathrust earthquake over an unprecedented
901 range of timescales, hence to constrain the nature of the underlying physical processes. We found
902 that early postseismic time series (minutes to months) can be explained by an afterslip
903 mechanism with a $p<1$ "Omori-like" signature for the velocities, in disagreement with the
904 prediction of a rate-and-state velocity-strengthening rheology for a frictional interface (which

would imply a $p \approx 1$). We argue instead that this early postseismic deformation results from a transient brittle creep mechanism within an unruptured section of the fault and its surroundings, corresponding to the cumulative effect of stress- and thermally activated local slip/deformation events. The regional variations of the *p*-value indicate that the area affected by the the Ibaraki-Oki aftershock is associated to a $p \sim 1$, that could be due to a negative thermal anomaly in this region.

At larger timescales (years), this transient afterslip mechanism underestimates the surface seaward motions observed by the land GPS stations. Afterslip can explain neither the landward motions observed by a few offshore GPS stations nor the exponential decay of the inland GPS velocities, that are likely a signature of viscoelastic mantellic deformation, which becomes significant at multiyear timescales.

In the future, it would be of upmost interest to extend such analysis to other megathrust earthquakes. This would allow to determine whether the characteristics of the Tohoku-Oki postseismic deformation are common or rather an exception.

Acknowledgments, Samples, and Data

This work has benefited from fruitful discussions with Hugo Perfettini.
This study has been supported by the Agence Nationale de la Recherche (ANR-17-CE31-0002-01) AtypicSSE project. The authors are very grateful to the Geospatial Information Authority of Japan (GSI) for making the GEONET GNSS data available. MR ackowledges the support of the Face fundation (Thomas Jefferson Fund TJF19-21).
The GNSS data processing presented in this paper was performed using the GRICAD infrastructure (https://gricad.univ-grenoble-alpes.fr), which is supported by Grenoble research communities.

Raw daily GNSS time series data are accessible on the Observatoire des Sciences de l'Univers de Grenoble website associated to the DOI: https://doi.org/10.17178/GNSS.products.Japan.
Kinematic GNSS time series are accessible on .. (in progress)
Static GNSS time series are accessible on .. (in progress)

References

Altamimi, Z., Rebischung, P., Métivier, L., & Collilieux, X. (2016). ITRF2014 : A new release of the International Terrestrial Reference Frame modeling nonlinear station motions: ITRF2014. Journal of Geophysical Research: Solid Earth, 121(8), 6109-6131. https://doi.org/10.1002/2016JB013098

Amitrano, D. (2003). Brittle-ductile transition and associated seismicity : Experimental and numerical studies and relationship with the b value: BRITTLE-DUCTILE TRANSITION AND SEISMICITY. Journal of Geophysical Research: Solid Earth, 108(B1). https://doi.org/10.1029/2001JB000680

Amitrano, D., Grasso, J.-R., & Hantz, D. (1999). From diffuse to localised damage through elastic interaction. Geophysical Research Letters, 26(14), 2109-2112. https://doi.org/10.1029/1999GL900388

Amitrano, D., & Helmstetter, A. (2006). Brittle creep, damage, and time to failure in rocks : TIME TO FAILURE IN ROCKS. Journal of Geophysical Research: Solid Earth, 111(B11), n/a-n/a. https://doi.org/10.1029/2005JB004252

Andrade, E. N. D. C. (1910). On the viscous flow in metals, and allied phenomena. Proceedings of the Royal Society of London. Series A, Containing Papers of a Mathematical and Physical Character, 84(567), 1-12. https://doi.org/10.1098/rspa.1910.0050

Baumberger, T., Berthoud, P., & Caroli, C. (1999). Physical analysis of the state- and rate-dependent friction law. II. Dynamic friction. Physical Review B, 60(6), 3928-3939. https://doi.org/10.1103/PhysRevB.60.3928

Bertiger, W., Desai, S. D., Haines, B., Harvey, N., Moore, A. W., Owen, S., & Weiss, J. P. (2010). Single receiver phase ambiguity resolution with GPS data. Journal of Geodesy, 84(5), 327-337. https://doi.org/10.1007/s00190-010-0371-9

Bilitza, D., Altadill, D., Zhang, Y., Mertens, C., Truhlik, V., Richards, P., McKinnell, L.-A., & Reinisch, B. (2014). The International Reference Ionosphere 2012 – a model of international collaboration. Journal of Space Weather and Space Climate, 4, A07. https://doi.org/10.1051/swsc/2014004

Boehm, J., Niell, A., Tregoning, P., & Schuh, H. (2006). Global Mapping Function (GMF) : A new empirical mapping function based on numerical weather model data. Geophysical Research

975 Letters, 33(7), L07304. https://doi.org/10.1029/2005GL025546
976 Bortz, A. B., Kalos, M. H., & Lebowitz, J. L. (1975). A New Algorithm for Monte Carlo
977 Simulation of king Spin Systems. Journal of Computational Physics, 17, 9.
978
979 Carter, N. L., & Kirby, S. H. (1978). Transient creep and semibrittle behavior of crystalline
980 rocks. 33.
981 Castellanos, D. F., & Zaiser, M. (2018). Avalanche Behavior in Creep Failure of Disordered
982 Materials. Physical Review Letters, 121(12), 125501.
983 https://doi.org/10.1103/PhysRevLett.121.125501
984 Choi, K. (2007). Improvements in GPS Precision : 10 Hz to One Day. 255.
985 Cottrell, A. H. (1952). The time laws of creep. Journal of the Mechanics and Physics of Solids,
986 1(1), 53-63. https://doi.org/10.1016/0022-5096(52)90006-9
987 Dieterich, J. H. (1979). Modeling of rock friction : 1. Experimental results and constitutive
988 equations. Journal of Geophysical Research, 84(B5), 2161.
989 https://doi.org/10.1029/JB084iB05p02161
990 Fukuda, J., Johnson, K. M., Larson, K. M., & Miyazaki, S. (2009). Fault friction parameters
991 inferred from the early stages of afterslip following the 2003 Tokachi-oki earthquake. Journal of
992 Geophysical Research, 114(B4). https://doi.org/10.1029/2008JB006166
993 Fukuda, J., Kato, A., Kato, N., & Aoki, Y. (2013). Are the frictional properties of creeping faults
994 persistent? Evidence from rapid afterslip following the 2011 Tohoku-oki earthquake:
995 AFTERSLIP AND FAULT FRICTION PROPERTIES. Geophysical Research Letters, 40(14),
996 3613-3617. https://doi.org/10.1002/grl.50713
997 Girard, L., Amitrano, D., & Weiss, J. (2010). Failure as a critical phenomenon in a progressive
998 damage model. Journal of Statistical Mechanics: Theory and Experiment, 2010(01), P01013.
999 https://doi.org/10.1088/1742-5468/2010/01/P01013
1000 Griggs, D. (1939). Creep of Rocks.
1001 Hayes, G. P., Moore, G. L., Portner, D. E., Hearne, M., Flamme, H., Furtney, M., & Smoczyk,
1002 G. M. (2018). Slab2, a comprehensive subduction zone geometry model. Science, 362(6410),
1003 58-61. https://doi.org/10.1126/science.aat4723
1004 Helmstetter, A., & Shaw, B. E. (2009). Afterslip and aftershocks in the rate-and-state friction

1005 law : AFTERSHOCKS AND RATE-AND-STATE FRICTION. Journal of Geophysical
1006 Research: Solid Earth, 114(B1). https://doi.org/10.1029/2007JB005077
1007 Heslot, F., Baumberger, T., Perrin, B., Caroli, B., & Caroli, C. (1994). Creep, stick-slip, and dry-
1008 friction dynamics : Experiments and a heuristic model. Physical Review E, 49(6), 4973-4988.
1009 https://doi.org/10.1103/PhysRevE.49.4973
1010 Hsu, Y.-J. (2006). Frictional Afterslip Following the 2005 Nias-Simeulue Earthquake, Sumatra.
1011 Science, 312(5782), 1921-1926. https://doi.org/10.1126/science.1126960
1012 Hu, Y., Bürgmann, R., Freymueller, J. T., Banerjee, P., & Wang, K. (2014). Contributions of
1013 poroelastic rebound and a weak volcanic arc to the postseismic deformation of the 2011 Tohoku
1014 earthquake. Earth, Planets and Space, 66(1), 106. https://doi.org/10.1186/1880-5981-66-106
1015 Ingleby, T., & Wright, T. J. (2017). Omori-like decay of postseismic velocities following
1016 continental earthquakes : OMORI DECAY OF POSTSEISMIC VELOCITIES. Geophysical
1017 Research Letters, 44(7), 3119-3130. https://doi.org/10.1002/2017GL072865
1018 Ji, Y., Yoshioka, S., Manea, V. C., Manea, M., & Matsumoto, T. (2016). Three-dimensional
1019 numerical modeling of thermal regime and slab dehydration beneath Kanto and Tohoku, Japan.
1020 Journal of Geophysical Research, 22.
1021 Langbein, J. (2006). Coseismic and initial postseismic deformation from the 2004 Parkfield,
1022 California earthquake, observed by GPS, EDM, creepmeters, and borehole strainmeters. 56.
1023 Lay, T. (2018). A review of the rupture characteristics of the 2011 Tohoku-oki Mw 9.1
1024 earthquake. Tectonophysics, 733, 4-36. https://doi.org/10.1016/j.tecto.2017.09.022
1025 Malservisi, R., Schwartz, S. Y., Voss, N., Protti, M., Gonzalez, V., Dixon, T. H., Jiang, Y.,
1026 Newman, A. V., Richardson, J., Walter, J. I., & Voyenko, D. (2015). Multiscale postseismic
1027 behavior on a megathrust : The 2012 Nicoya earthquake, Costa Rica: POSTSEISMIC 2012
1028 NICOYA EARTHQUAKE. Geochemistry, Geophysics, Geosystems, 16(6), 1848-1864.
1029 https://doi.org/10.1002/2015GC005794
1030 Marill, L., Marsan, D., Socquet, A., Radiguet, M., Cotte, N., & Rousset, B. (2021). 14-year
1031 acceleration along the Japan Trench. Journal of Geophysical Research: Solid Earth.
1032 https://doi.org/10.1029/2020JB021226
1033 Marone, C. (1998). Laboratory-Derived Friction Laws and Their Application to Seismic
1034 Faulting. Annual Review of Earth and Planetary Sciences, 26(1), 643-696.
1035 https://doi.org/10.1146/annurev.earth.26.1.643

1036 Marone, C. J., Scholtz, C. H., & Bilham, R. (1991). On the mechanics of earthquake afterslip.
1037 Journal of Geophysical Research, 96(B5), 8441. https://doi.org/10.1029/91JB00275
1038 Marquez-Azua, B., & DeMets, C. (2003). Crustal velocity field of Mexico from continuous GPS
1039 measurements, 1993 to June 2001 : Implications for the neotectonics of Mexico. 20.
1040 Miyazaki, S., & Larson, K. M. (2008). Coseismic and early postseismic slip for the 2003
1041 Tokachi-oki earthquake sequence inferred from GPS data. Geophysical Research Letters, 35(4).
1042 https://doi.org/10.1029/2007GL032309
1043 Montési, L. G. J. (2004). Controls of shear zone rheology and tectonic loading on postseismic
1044 creep : TIME DEPENDENCE OF POSTSEISMIC CREEP. Journal of Geophysical Research:
1045 Solid Earth, 109(B10). https://doi.org/10.1029/2003JB002925
1046 Morikami, S., & Mitsui, Y. (2020). Omori-like slow decay ($p < 1$) of postseismic displacement
1047 rates following the 2011 Tohoku megathrust earthquake. Earth, Planets and Space, 72(1), 37.
1048 https://doi.org/10.1186/s40623-020-01162-w
1049 Munekane, H. (2012). Coseismic and early postseismic slips associated with the 2011 off the
1050 Pacific coast of Tohoku Earthquake sequence : EOF analysis of GPS kinematic time series.
1051 Earth, Planets and Space, 64(12), 1077-1091. https://doi.org/10.5047/eps.2012.07.009
1052 Nishimura, T., Munekane, H., & Yarai, H. (2011). The 2011 off the Pacific coast of Tohoku
1053 Earthquake and its aftershocks observed by GEONET. Earth, Planets and Space, 63(7), 631-363.
1054 https://doi.org/10.5047/eps.2011.06.025
1055 Okada, Y. (1992). Internal deformation due to shear and tensile faults in a half-space. Bulletin of
1056 the Seismological Society of America, 82(2), 1018-1040.
1057 Ozawa, S., Nishimura, T., Munekane, H., Suito, H., Kobayashi, T., Tobita, M., & Imakiire, T.
1058 (2012). Preceding, coseismic, and postseismic slips of the 2011 Tohoku earthquake, Japan :
1059 AFTERSLIP OF THE TOHOKU EARTHQUAKE. Journal of Geophysical Research: Solid
1060 Earth, 117(B7), n/a-n/a. https://doi.org/10.1029/2011JB009120
1061 Perfettini, H., & Ampuero, J.-P. (2008). Dynamics of a velocity strengthening fault region :
1062 Implications for slow earthquakes and postseismic slip. Journal of Geophysical Research,
1063 113(B9). https://doi.org/10.1029/2007JB005398
1064 Perfettini, H., & Avouac, J. P. (2014). The seismic cycle in the area of the 2011 M $_w$ 9.0
1065 Tohoku-Oki earthquake. Journal of Geophysical Research: Solid Earth, 119(5), 4469-4515.
1066 https://doi.org/10.1002/2013JB010697

1067 Perfettini, H., & Avouac, J.-P. (2004). Postseismic relaxation driven by brittle creep : A possible
1068 mechanism to reconcile geodetic measurements and the decay rate of aftershocks, application to
1069 the Chi-Chi earthquake, Taiwan: DYNAMICS OF BRITTLE CREEP. Journal of Geophysical
1070 Research: Solid Earth, 109(B2). https://doi.org/10.1029/2003JB002488
1071 Perfettini, H., Avouac, J.-P., Tavera, H., Kositsky, A., Nocquet, J.-M., Bondoux, F., Chlieh, M.,
1072 Sladen, A., Audin, L., Farber, D. L., & Soler, P. (2010). Seismic and aseismic slip on the Central
1073 Peru megathrust. Nature, 465(7294), 78-81. https://doi.org/10.1038/nature09062
1074 Radiguet, M., Cotton, F., Vergnolle, M., Campillo, M., Valette, B., Kostoglodov, V., & Cotte, N.
1075 (2011). Spatial and temporal evolution of a long term slow slip event : The 2006 Guerrero Slow
1076 Slip Event: Evolution of the 2006 Guerrero SSE. Geophysical Journal International, 184(2),
1077 816-828. https://doi.org/10.1111/j.1365-246X.2010.04866.x
1078 Radiguet, M., Perfettini, H., Cotte, N., Gualandi, A., Valette, B., Kostoglodov, V., Lhomme, T.,
1079 Walpersdorf, A., Cabral Cano, E., & Campillo, M. (2016). Triggering of the 2014 M w 7.3
1080 Papanoa earthquake by a slow slip event in Guerrero, Mexico. Nature Geoscience, 9(11),
1081 829-833. https://doi.org/10.1038/ngeo2817
1082 Rice, J. R., & Tse, S. T. (1986). Dynamic motion of a single degree of freedom system following
1083 a rate and state dependent friction law. 10.
1084 Savage, J. C. (2007). Postseismic relaxation associated with transient creep rheology. Journal of
1085 Geophysical Research, 112(B5), B05412. https://doi.org/10.1029/2006JB004688
1086 Savage, J. C., Svarc, J. L., & Yu, S.-B. (2005). Postseismic relaxation and transient creep :
1087 POSTSEISMIC RELAXATION AND CREEP. Journal of Geophysical Research: Solid Earth,
1088 110(B11). https://doi.org/10.1029/2005JB003687
1089 Scholz, C. H. (1968). Mechanism of creep in brittle rock. Journal of Geophysical Research,
1090 73(10), 3295-3302. https://doi.org/10.1029/JB073i010p03295
1091 Selle, C., & Desai, S. (2016). Optimization of tropospheric delay estimation parameters by
1092 comparison of GPS-based precipitable water vapor estimates with microwave radiometer
1093 measurements. 17.
1094 Sobrero, F. S., Bevis, M., Gómez, D. D., & Wang, F. (2020). Logarithmic and exponential
1095 transients in GNSS trajectory models as indicators of dominant processes in postseismic
1096 deformation. Journal of Geodesy, 94(9), 84. https://doi.org/10.1007/s00190-020-01413-4
1097 Spiridonov, E. A., & Vinogradova, O. Yu. (2020). Oceanic Tide Model FES2014b : Comparison

with Gravity Measurements. Izvestiya, Atmospheric and Oceanic Physics, 56(11), 1432-1446. https://doi.org/10.1134/S0001433820110092

Sun, T., & Wang, K. (2015). Viscoelastic relaxation following subduction earthquakes and its effects on afterslip determination. Journal of Geophysical Research: Solid Earth, 120(2), 1329-1344. https://doi.org/10.1002/2014JB011707

Sun, T., Wang, K., Iinuma, T., Hino, R., He, J., Fujimoto, H., Kido, M., Osada, Y., Miura, S., Ohta, Y., & Hu, Y. (2014). Prevalence of viscoelastic relaxation after the 2011 Tohoku-oki earthquake. Nature, 514. https://doi.org/10.1038/nature13778

Tajima, F., Mori, J., & Kennett, B. L. N. (2013). A review of the 2011 Tohoku-Oki earthquake (Mw 9.0) : Large-scale rupture across heterogeneous plate coupling. Tectonophysics, 586, 15-34. https://doi.org/10.1016/j.tecto.2012.09.014

Tobita, M. (2016). Combined logarithmic and exponential function model for fitting postseismic GNSS time series after 2011 Tohoku-Oki earthquake. Earth, Planets and Space, 68(1), 41. https://doi.org/10.1186/s40623-016-0422-4

Tsang, L. L. H., Vergnolle, M., Twardzik, C., Sladen, A., Nocquet, J.-M., Rolandone, F., Agurto-Detzel, H., Cavalié, O., Jarrin, P., & Mothes, P. (2019). Imaging rapid early afterslip of the 2016 Pedernales earthquake, Ecuador. Earth and Planetary Science Letters, 524, 115724. https://doi.org/10.1016/j.epsl.2019.115724

Twardzik, C., Vergnolle, M., Sladen, A., & Avallone, A. (2019). Unravelling the contribution of early postseismic deformation using sub-daily GNSS positioning. Scientific Reports, 9(1). https://doi.org/10.1038/s41598-019-39038-z

Wang, K., Hu, Y., & He, J. (2012). Deformation cycles of subduction earthquakes in a viscoelastic Earth. Nature, 484(7394), 327-332. https://doi.org/10.1038/nature11032

Wang, K., Sun, T., Brown, L., Hino, R., Tomita, F., Kido, M., Iinuma, T., Kodaira, S., & Fujiwara, T. (2018). Learning from crustal deformation associated with the M9 2011 Tohoku-oki earthquake. Geosphere, 14(2), 552-571. https://doi.org/10.1130/GES01531.1

Zumberge, J. F., Heflin, M. B., Jefferson, D. C., Watkins, M. M., & Webb, F. H. (1997). Precise point positioning for the efficient and robust analysis of GPS data from large networks. Journal of Geophysical Research: Solid Earth, 102(B3), 5005-5017. https://doi.org/10.1029/96JB03860